To the Graduate Council:

I am submitting herewith a dissertation written by Seonghwan Kim entitled "Characterization of dynamic response of AFM cantilevers for microscale thermofluidic and biophysical sensors." I have examined the final electronic copy of this dissertation for form and content and recommended that it be accepted in partial fulfillment of the requirements for the degree of Doctor of Philosophy, with a major in Mechanical Engineering.

Kenneth D. Kihm
Major Professor

We have read this dissertation
and recommend its acceptance:

Anthony E. English

Thomas G. Thundat

Dongjun Lee

Timothy G. Rials

Accepted for the council:

Carolyn R. Hodges
Vice Provost and Dean of
Graduate Studies

(Original signatures are on file with official student record)

Characterization of dynamic response of AFM cantilevers for microscale thermofluidic and biophysical sensors

A Dissertation Presented

for the

Doctor of Philosophy Degree

The University of Tennessee, Knoxville

Seonghwan Kim

August 2008

DEDICATION

To my parents (Sam Kwan Kim & Bok Soon Chang), my family (wife: Mi Ryoung Shin, daughter: Kyoung-eun Kim, & sons: Caleb K. Kim, Joshua K. Kim), and my precious Lord Jesus Christ.

ACKNOWLEDGEMENTS

I would like to give my sincere appreciation and gratitude to my advisor Dr. Kenneth D. Kihm for his continuous support, encouragement, valuable advices, and stimulating discussions throughout the course of this study. Also I would like to express my heartfelt gratitude to my co-advisor, Dr. Anthony E. English, for his valuable guidance and constant support throughout this study. I would like to thank my dissertation committee members, Dr. Thomas G. Thundat, Dr. Timothy G. Rials, and Dr. Dongjun Lee for their advice and constructive comments and voluntary services.

Special thanks are expressed to the MINSFET Lab former and current members who worked and spent time with, Dr. Chanhee Chon, Dr. Sokwon Paik, Dr. Jaesung Park, Dr. Changkyoung Choi, Mr. Iltai Kim, Mr. Chuck Margrav, and Mr. Joseph Tipton.

I wish to extend my thanks to my parents and parents-in-law for their continuing support and prayer. Lastly, I would like to express my love and appreciation to my wonderful wife, Mi Ryoung Shin for her sacrifice, patience, trust, and love.

If I speak in the tongues of men and of angels, but have not love, I am only a resounding gong or a clanging cymbal. If I have the gift of prophecy and can fathom all mysteries and all knowledge, and if I have a faith that can move mountains, but have not love, I am nothing. If I give all I possess to the poor and surrender my body to the flames, but have not love, I gain nothing. And now these three remain: faith, hope and love. But the greatest of these is love. (1 Corinthians 13:1-3, 13)

ABSTRACT

My doctoral research has focused on the characterization of dynamic response of atomic force microscope (AFM) cantilevers for thermofluidic and biophysical sensors, a novel scanning thermal microscopy technique development using a tipless microcantilever to investigate micro/nanoscale transport properties in liquid, and the characterization of the surface nanomechanical properties of biocompatible polyelectrolyte hydrogels with AFM for biomedical applications.

The temperature effects on Sader's viscous model for multilayered microcantilevers immersed in an aqueous medium were experimentally verified as a preliminary work. Next, temperature dependence of the near-wall oscillation of microcantilevers submerged in an aqueous medium was investigated to explore the possibility of a near-wall thermometry sensor. By correlating the frequency response of a microcantilever immersed in an aqueous medium near a solid surface (within the width of a microcantilever) with the surrounding liquid temperature, the near-wall region microscale temperature distributions at the probing site were successfully determined. For biological applications, this work has been extended to examine the effect of adsorption-induced surface stress change on the stiffness of a microcantilever immersed in saline solution with varying salt concentrations. It was found that adsorption-induced surface stress change increased the stiffness of a microcantilever in saline solution with increasing salt concentration ranging from 0 to 2 molality.

The surface nanomechanical properties of 2-hydroxyethyl methacrylate (HEMA) and 2-methacryloxyethyl trimethyl ammonium chloride (MAETAC) copolymer hydrogels were probed using AFM. The HEMA-MAETAC polyelectrolyte hydrogels

with increasing positive charge concentrations ranging from 0 to 400 mM in increments of 40 mM, were fabricated using different proportions of HEMA and MAETAC monomers. Increasing proportions of positively charged MAETAC monomers produced hydrogels with increasingly swollen states and correspondingly decreasing measures of surface elasticity, or Young's modulus. The attachment of porcine pulmonary artery endothelial cells (PPAECs) increased with increasing prepared hydrogel charge concentration and subsequently decreasing surface elasticity.

Keywords: Atomic Force Microscope (AFM), Microcantilever, Thermofluidic sensor, Hydrogel, Surface elasticity

TABLE OF CONTENTS

Characterization of dynamic response of AFM cantilevers for microscale thermofluidic and biophysical sensors

CHAPTER 1 Introduction **1**

1.1 Atomic Force Microscope (AFM) **1**
1.2 Microcantilever Sensors **3**
1.3 Motivation and Objectives **4**
1.4 Organization of the Study **5**

CHAPTER 2 Temperature effects on the frequency response of a microcantilever immersed in aqueous medium **7**

2.1 Introduction **7**
2.2 Theoretical Background **8**
2.3 Experimental Methods **10**
2.4 Results and Discussion **16**
2.5 Conclusion **31**

CHAPTER 3 Effect of adsorption-induced surface stress change on the frequency response of a microcantilever immersed in saline solution **33**

3.1 Introduction **33**
3.2 Theoretical Background **34**
3.3 Experimental Methods **38**
3.4 Results and Discussion **39**
3.5 Conclusion **44**

CHAPTER 4 Scanning thermal microscopy (SThM) technique in liquid medium **45**

4.1 Introduction **45**
4.2 Methods and Materials **47**
4.3 Results and Discussion **54**
4.4 Conclusion **59**

CHAPTER 5 Atomic Force Spectroscopy (AFS) for the surface nanomechanical property measurements of polyelectrolyte hydrogels **61**

5.1 Introduction **61**
5.2 Methods and Materials **63**
5.3 Results and Discussion **66**
5.4 Conclusion **80**

CHAPTER 6 Conclusion **81**

REFERENCES **84**

APPENDIX **96**

VITA **107**

LIST OF TABLES

2.1	Physical dimensions and properties of three different tested tipless microcantilevers.	12
2.2	Physical dimensions and properties of three different tested tipless microcantilevers.	15
3.1	The adsorbed mass of sodium ions of the four tested cantilevers for the different NaCl concentrations.	36
3.2	Physical dimensions and properties of four different tested microcantilevers.	37
3.3	The spring constant changes of the tested microcantilevers for the different NaCl concentrations.	41

LIST OF FIGURES

1.1 A schematic drawing of the typical AFM setup. 2

2.1 Theoretical predictions and experimental verifications of the thermally induced resonance frequency spectra and the *Q*-factor for NSC12-C1 cantilever immersed in de-ionized water: (a) Predictions based on the extended Sader's viscous model for individual contributions to the net peak resonance response frequency shifts ($\Delta f = \Delta f_\eta + \Delta f_\rho + \Delta f_E$) from the lower-end frequency at 10 °C due to the decrease in the liquid viscosity, Δf_η, the decrease in the liquid density, Δf_ρ, and the slight decrease of Young's modulus of cantilever, Δf_E, with increasing liquid temperature (b) Calculated power spectral density (PSD) of the slope of the cantilever immersed in de-ionized water at three selected temperatures of 10, 40 and 70 °C (c) Measured power spectral density (PSD) of the slope of the cantilever immersed in de-ionized water at three selected temperatures of 10, 40 and 70 °C (d) Measured peak resonance response frequencies and the corresponding *Q*-factors at temperatures ranging from 10 to 70 °C. The error bars indicate 95% confidence intervals of measured data. 17-20

2.2 Magnitudes of the peak resonance response frequency shifts as functions of the temperature differential from the lower-end 10 °C for the three tested TL-NCH1, NSC12-B, and NSC12-C1 cantilevers. The curves represent theoretical predictions by the extended Sader's viscous model and the symbols represent the averaged shifts of the peak resonance response frequencies with the error bars showing 95% confidence intervals of measured data. 22

2.3 Theoretical predictions of the thermally induced resonance frequency shifts for TL-NCH2 cantilever immersed in de-ionized water near a solid surface. Predictions based on modification of Sader's model for individual contributions to the net peak resonance response frequency 24

shifts ($\Delta f = \Delta f_\eta + \Delta f_\rho + \Delta f_E$), the decrease in dissipative effect by the liquid viscosity Δf_η, the decrease in inertial effect by the liquid density Δf_ρ, and the slight decrease of Young's modulus of cantilever Δf_E, with increasing liquid temperature at different normalized separation distances H = 0.1 and 1.0.

2.4 Calculated and measured peak resonance response frequency shifts from the lower-end frequency at 30 °C as functions of temperature for TL-NCH2 cantilever immersed in de-ionized water at different separation distances. The curves represent theoretical predictions by the modified Sader's model, and the symbols represent the averaged shifts of the peak resonance response frequencies with the error bar showing 95% confidence intervals of measured data. Note that the separation distance H is defined based on the tip-to-wall distance, while the practical cantilever is inclined at a small angle from the horizon. 26

2.5 Calculated near-wall thermal sensitivity $\Delta f/\Delta T$ at H = 0.5 of microcantilevers made of silicon as functions of h/L^2 for three different widths b = 20, 30, and 40 μm. 28

2.6 Magnitudes of the peak resonance response frequency shifts as functions of the temperature differential from the lower-end 30 °C for the three tested TL-NCH2, NSC12-C2, and NSC12-F cantilevers. The curves represent theoretical predictions at H = 1.0, and the three families of symbols (triangles, squares, and circles) represent the average shifts of the peak resonance response frequencies measured at three different separation distances H = 0.1, 0.3, and 1.0, respectively. 30

3.1 Theoretical predictions and experimental measurements of the resonance frequency shifts in saline solution from the reference frequency in de-ionized water as functions of NaCl concentration for the four tested cantilevers. The four curves show calculated frequency shifts by the Sader's viscous model assuming both δk and δm are zero and each symbol represents the averaged frequency shifts from ten (10) measurements, with the error bar corresponding to 95% confidence 40

interval of measured data.

3.2 Measured and predicted NaCl concentration detection sensitivity, $\Delta f/\Delta C$, for the four tested cantilevers as functions of h/L^2 assuming both δk and δm are zero in theoretical calculation. 42

4.1 Experimental near-wall correlation of the microcantilever peak resonance response frequency with aqueous medium temperature at four different separation distances (z = 5, 10, 20, and 40 µm) between the lower end of the cantilever and the glass substrate surface. 48

4.2 (a) A micro-line heater design. (b) Schematic illustration of the microscale thermal environment with a microheater. 50

4.3 A schematic drawing of the near-field microscale thermometry in aqueous liquid using a tipless microcantilever and a microphotograph of the micro-line heater and cantilever. 51

4.4 Two-dimensional computational simulation domain of the microscale thermal environment and the detailed prediction of the temperature distribution. 53

4.5 Transient temperature measurements at z = 40 µm while the microheater temperature T_h was maintained at 50 °C, 70 °C, or 90 °C. 55

4.6 Measured and calculated steady-state temperature profiles in the vicinity of the microheater surface. 57

4.7 Calculated near-wall thermal sensitivity of silicon microcantilevers as functions of h/L^2 for three different widths b = 20, 30, and 40 µm. 58

5.1 HEMA-MAETAC equilibrium swelling behavior as a function of copolymer hydrogel charge with a fixed of 154 mM NaCl bath salt concentration. Adding increasing proportions of positively charged monomers produces increasingly swollen states. Inset scale bars = 2 µm. 67

5.2 Force-displacement curves for a representative hydrogels in an approaching and retracting cycle. (a) Neutral HEMA (b) +200 mM HEMA-MAETAC (c) +400mM HEMA-MAETAC. The approach and retract curve hysteresis and the initial approach curve deflection occur in association with increasing charged monomer concentration. 69

5.3 Indentation depth for a given cantilever deflection versus initially prepared hydrogel charged monomer concentration using a retracting curve analysis. The error bars represent the standard deviation of fifty 71

measurements at five different locations (ten at each location) over the hydrogel surface.

5.4 Young's modulus versus indentation depth using a retracting curve analysis. 72

5.5 HEMA-MAETAC force spectroscopy estimates of the surface elasticity. Adding increasing proportions of positively charged monomers produces a decrease in the surface elasticity. The error bars represent the standard deviation of a total fifty measurements at five different locations (ten at each location) over the hydrogel surface. The four sets of data represent hydrogels that were equilibrated in 154 mM NaCl, M199 media with FBS, M199 media without FBS but containing 25 mM HEPES buffer, and M199 media with FBS containing 25 mM HEPES buffer. 74

5.6 Endothelial cell morphologies as a function of prepared hydrogel charge after 20 hours of growth. Hydrogels prepared with 0, +40, or +80 mM MAETAC resist cellular attachment. Hydrogels prepared with charged monomer concentrations between +120 and +400 mM promote cellular attachment. Scale bars = 100 µm. 76

CHAPTER 1

Introduction

1.1 Atomic Force Microscope (AFM)

An atomic force microscope, developed by Binnig, Gerber, and Quate in 1986 [1] , is a kind of scanning probe microscope using a sharp physical probe that scans across a specimen to mainly get the surface nanotopography by monitoring interatomic forces between probe and specimen. The interatomic forces between probe and specimen are detected via the deflection or the resonance frequency shift of a microcantilever which is fabricated with a very sharp probe tip. These forces, then, are used to control the cantilever z-position to record surface nanotopography or to probe surface nanomechanical characteristics of samples. Comparing to conventional optical microscopes, AFM dramatically improved spatial resolutions in surface topographical imaging of conducting and non-conducting objects to sub nanometer scale resolution [2]. In addition, AFM also allowed local intermolecular force detection below the picoNewton level with a high resolution, thus opened new realm of force spectroscopy of biological surfaces [3].

A general AFM system consists of a microcantilever with a sharp probe tip which works as a force sensor, a piezoelectric scanner which controls the x-y-z movements of a sample with sub nanometer accuracy, a laser and a position sensitive detector which measures the deflection of a cantilever, feedback electronics which control z-position of a sample, and a computer which controls system and performs data acquisition, display,

and analysis. Figure 1.1 illustrates the schematic of a typical AFM setup. The deflection

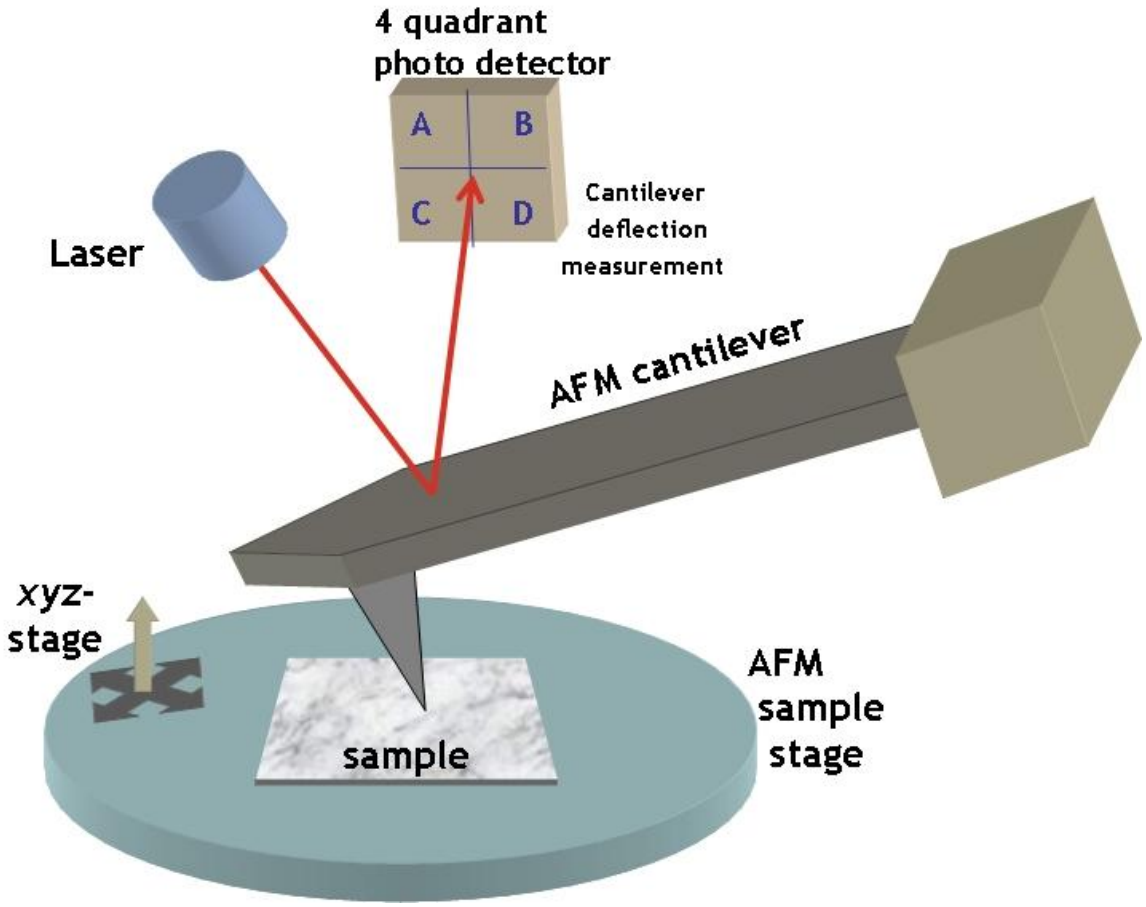

Figure 1.1: A schematic drawing of the typical AFM setup [4].

or the frequency response of a microcantilever with a sharp probe tip is measured by reflecting a laser beam off the backside of the cantilever and acquiring optical signals with a position sensitive detector while a sharp probe tip is scanning over the surface of the sample. These collected optical signals are converted to electrical signals for feedback electronics to maintain constant cantilever deflection (constant-force mode AFM imaging) or constant cantilever vibration amplitude (non-contact mode AFM imaging) by changing z distance between tip and sample. Then, images are generated and displayed from the piezoelectric scanner's x-y-z motions.

1.2 Microcantilever Sensors

A microcantilever is a micrometer-sized single clamped suspended beam. Typical dimensions of microcantilevers are order of 100 μm long, 10 μm wide and 1 μm thick. Advanced microfabrication techniques made it possible to fabricate very precise and reliable microcantilevers at low cost. Especially, the development of microcantilevers for AFM has been a major driving force for the fabrication of precise and reliable microcantilevers in various shapes and sizes. These microcantilevers have been used for various scanning probe microscopes (SPM) and diverse microelectromechanical systems (MEMS), including sensors and actuators, for over two decades [5-9]. They have been exploited as mechanical transducers for biological, chemical, and physical sensing applications in previous studies [10-12]. The dynamic frequency responses and the static deflection of a microcantilever are two main transduction mechanisms for microcantilever sensors. The operation modes of microcantilever sensors are classified with these two transduction mechanisms. In dynamic mode, the frequency responses of a

microcantilever-peak resonance response frequency, quality factor, amplitude, and phase-need to be simultaneously measured and in static mode, the deflection of a microcantilever need to be precisely measured for sensing applications. These frequency responses and deflection of a microcantilever can be measured by various readout techniques including optical lever, piezoresistive, piezoelectric, capacitance, or electron tunneling methods with sufficient precision [13]. Two most important figures of merit of microcantilever sensors are sensitivity and specificity. Usually by miniaturization and optimization, high sensitivity is achieved and by coating some material on top of a microcantilever, specificity is realized for a certain type of physical, biological or chemical sensing applications [14].

1.3 Motivation and Objectives

Microcantilever sensors are recognized as a versatile platform for the next generation physical, biological and chemical sensors. It is anticipated that microcantilever sensors provide real-time, *in situ* measurements of physical, biological, and chemical properties of fluids. In order to understand micro/nanoscale fluidics and energy transport phenomena, it is essential to detect micro/nanoscale transport properties such as viscosity, density, temperature, and concentration in liquid without being disturbed by any foreign labels. Foreign materials can affect or alter transport properties of liquid and cause measurement inaccuracy. Therefore, a microcantilever is employed as a sensing platform for micro/nanoscale liquid property detection and dynamic frequency responses of a microcantilever in liquid is investigated. This study aims to reveal the fundamental physical understandings of temperature and concentration effects on dynamic responses

of a microcantilever in liquid and provide a novel near-wall scanning thermal microscopy technique in liquid.

In addition, AFM cantilever sensor application is extended to biophysics area. The development of AFM and the subsequent development of atomic force spectroscopy (AFS) [15] have made it possible to probe the surface mechanical properties of materials at a submicron scale. This is potentially significant because the surface nanomechanical properties of natural and synthetic hydrogels play a critical role in their use as biomaterials. As a result, the application of AFS technology to soft hydrogel biomaterials has a number of important applications in medicine and biomedical engineering. The mechanical properties of synthetic hydrogels reflect the complicated combination of the neutral and charged monomer concentrations, the solvent quality, the chemical dissociation effects, and many other factors [16-21]. These competing and non-linear effects make it challenging to predict and understand the mechanical properties of these materials. In particular, the incorporation of charged monomers into an otherwise neutral and inert background has been exploited in a number of studies to promote cell adhesion and proliferation [22-25]. Thus, this study also aims to precisely characterize the surface nanomechanical properties of polyelectrolyte hydrogels in liquid medium and reveal the biophysical implication of these properties on cell-substrate interactions.

1.4 Organization of the Study

This study consists of two fundamental investigations of dynamic responses of a microcantilever in liquid mediums and two practical applications of AFM cantilevers for thermofluidic and biophysical sensors. Chapter 2 presents a study of temperature effects

on the frequency response of a microcantilever in aqueous medium, which includes the extension of Sader's viscous model and thermal experiments designed to elucidate the roles of liquid viscosity, liquid density, elasticity of a microcantilever, and separation distance between a cantilever and a solid surface on the frequency response of a microcantilever by precisely controlling surrounding liquid temperature and separation distance. Chapter 3 presents a study of salt concentration effects on the frequency response of a microcantilever in saline solution, which includes the extension of Sader's viscous model and experiments designed to elucidate the roles of NaCl concentration on the stiffness of a microcantilever and subsequent frequency response of a microcantilever in saline solution by precisely controlling salt concentration. Chapter 4 shows a practical application of AFM cantilever sensor in the form of scanning thermal microscopy (SThM) technique in liquid medium. By measuring microscale temperature distribution in aqueous medium and comparing it with numerical calculation, a novel SThM concept was successfully proved and validated. Chapter 5 discusses atomic force spectroscopy for the surface nanomechanical property measurements of polyelectrolyte hydrogels. The surface elasticities of polyelectrolyte hydrogels in liquid medium are characterized and cellular attachment experiment was performed to investigate the biophysical implication of these properties on cell-substrate interactions. Chapter 6 presents the conclusions derived from this study and provides recommendations for further research.

CHAPTER 2

Temperature effects on the frequency response of a microcantilever immersed in aqueous medium

2.1 Introduction

Microcantilevers have been used for atomic force microscope (AFM) and diverse microelectromechanical systems (MEMS), including sensors and actuators, for over two decades and have been exploited as mechanical transducers for biological, chemical, and physical sensing applications in previous studies [26-33]. The peak resonance response frequency shift and the deflection of a microcantilever are two main transduction mechanisms for microcantilever sensors. Especially, the peak resonance response frequency and the quality factor of a microcantilever are two main dynamic characteristics that are very sensitive to density and viscosity of the surrounding fluid and the proximity of a microcantilever to a solid surface [34]. Various sensors based on these mechanisms have been developed for detection in gaseous environments. However, for liquid environments, the development of microcantilever sensors has suffered from several drawbacks including a low quality factor, its generally narrow dynamic range, parasitic deflection, and long-term drift [35].

The potentially extensive needs of microcantilever sensors in biological and chemical applications make it essential to overcome these complications occurring in liquid environments. Although several research groups have published progressive results for the enhancement of the quality factor [35-37] and for the improvement of the deflection transduction techniques [38], the dependence of the peak resonance response

frequency shift on the surrounding temperature changes in liquid environments has not been systematically examined. In addition, the dependence of the peak resonance response frequency shift of a microcantilever near a solid surface on the surrounding temperature changes in liquid environments has not been systematically examined. Almost all published theoretical and experimental studies of microcantilever sensors immersed in liquid have assumed or specified a constant temperature condition.

2.2 Theoretical Background

Sader and Green and Sader presented theoretical models [39, 40] to predict thermally-driven resonance frequencies of a microcantilever immersed in different viscous fluids. Their models showed acceptable agreement with experiments for the case of a constant temperature for microcantilevers with aspect ratios (*AR* = cantilever length/cantilever width) ranging from 4 to 14 [41]. They also reported feasibility of a simultaneous fluid viscosity and density determination sensor using a single rectangular microcantilever in a constant temperature condition [42]. Recently, Green and Sader modified their previous theoretical models to predict thermally driven resonance frequencies of a microcantilever immersed in a fluid near a solid surface [43]. Their model includes both inertial and dissipative effects in fluid to account for variations of frequency responses observed when a cantilever is brought close to a solid surface. This study elucidated the basic mechanisms of the broadening of the resonance peaks and the peak resonance response frequency shifts to lower frequencies as the microcantilever beam/surface separation distance decreased.

In order to comprehensively examine the temperature effect on the frequency

response of a microcantilever immersed in a fluid near or far away from a solid surface, the Sader's model is extended to individually account for the liquid viscosity $\eta(T)$, density $\rho(T)$, and the Young's modulus of microcantilever *E(T)* as functional forms of temperature. For de-ionized water, the functional forms of the corresponding properties are given as [44]

$$\eta(T) = \eta_0 e^{-1.70 - 45.306 + 7.00 z^2}, \qquad z = \frac{273}{T} \qquad \eta_0 = 1.788\times10^{-3}\ kg m^{-1} s^{-1} \tag{1}$$

$$\rho(T) = 1000 - 0.0178\left|T - 273\right|^{1.7}\ kg\, m^{-3}, \tag{2}$$

The thermal dependence of Young's modulus *dE/dT* of silicon remains nearly constant as -8.7 MPaK^{-1} for the tested water temperature range from 10 to 70 °C. In other words, the Young's modulus *E* decreases linearly with increasing temperature. The coefficient of thermal expansion α of silicon is invariant as 2.6×10^{-6} K^{-1} [45-47]. The thermal dependence of Young's modulus *dE/dT* of the coated gold layer is given as -24.0 MPaK^{-1} and α of gold is given as 14.2×10^{-6} K^{-1} [48].

Based on the thermal sensitivity equation for a single layer cantilever [48], the fundamental resonant frequency in vacuum ω_{vac} is formulated as:

$$\omega_{vac}(T) = \omega_{vac}(T_0)\sqrt{\frac{E(T_0) + \frac{dE}{dT}(T - T_0)}{E(T_0)}}\, e^{\frac{\alpha}{2}(T - T_0)}, \tag{3}$$

where *T* is the surrounding medium temperature in which the cantilever is submerged and T_0 is the reference temperature. The fundamental resonant frequency at the reference temperature $\omega_{vac}(T_0)$ is provided by the Sader's Simple Harmonic Oscillator (SHO) model using the readily measured peak resonance response frequency and the *Q*-factor in

air [41]. As a reference point, Young's modulus $E(T_0)$ of silicon is given as 167 GPa at T_0 = 20 ºC [46].

For a two-layered cantilever, such as a gold-coated silicon substrate neglecting the chromium adhesion layer, the fundamental resonance frequency $\omega_{vac,1}$ is given by the Reuss model as [48]

$$\omega_{vac,1}(T) = \omega_{vac}(T)(1+x)^2 \sqrt{\frac{E_a(T)\rho_s}{(E_a(T)+xE_s(T))(\rho_s + x\rho_a)}}, \tag{4}$$

where $\omega_{vac}(T)$ is the fundamental resonance frequency of the uncoated or single-layered cantilever at T in vacuum as given in Eq. (3), the thickness ratio $x = t_a/t_s$ with t_a being the gold coating thickness and t_s being the substrate thickness. $E_s(T)$ and $E_a(T)$ represent the Young's modulus of the cantilever substrate (Si) and the coated material (Au), respectively. ρ_s and ρ_a are the mass density of the substrate (Si) and the coated (Au) material, respectively.

Therefore, for the case of a single-layered cantilever, the extended Sader's viscous model constitutes Eqs. (1) to (3), and for the case of a double-layered cantilever the model constitutes Eqs. (1) to (4). Taking all of these equations into consideration along with the original Sader's model equations [39, 43] gives a closed form solution for the resonance frequency spectra as a function of temperature. A detailed mathematical derivation of the extended Sader's viscous model is given in Appendix.

2.3 Experimental Methods

First, well-controlled thermal experiments were performed to systematically validate the temperature effects on the existing theory primarily developed by the Sader's

group. For a microcantilever immersed in aqueous medium far away from a solid surface (distance between a microcantilever and a solid surface is larger than the width of a microcantilever), a wide range of temperatures from 10 to 70 °C is tested to observe changes in the viscosity and density of de-ionized water as well as the stiffness of a microcantilever.

Experiments are conducted to measure the flexural vibration frequency response for three different microcantilevers immersed in de-ionized water at different temperatures. In particular, three cantilevers, with $AR < 4$, are tested to explore the lower limit of AR validating the Sader's viscous model in which an infinitely long cantilever was assumed. Three different tipless silicon microcantilevers are selected for testing and their physical layouts, material properties, and fundamental resonance frequencies in air at 20 °C are shown in Table 2.1. The plan view dimensions (Length L and width b) are measured using a calibrated optical microscope by the author. The manufacturers provided the thicknesses (h) data showing 20% variations from the nominal value for TL-NCH1 and 15% variations for NSC12 series microcantilevers. TL-NCH1 is a single-layered cantilever of an aspect ratio of approximately 3.0, with the highest spring constant k among the three. 400-nm and 100-nm thick gold layers are additionally coated on NSC12-B and NSC12-C1 single-layered silicon cantilevers, respectively, using an e-beam evaporator facility at the University of Tennessee, Knoxville. A calibrated quartz crystal microbalance (QCM) sensor inside the e-beam evaporator measures the layer thicknesses with one angstrom accuracy. Direct scanning of AFM also verifies the thickness measurement accuracy. Note that the aspect ratio of NSC12-B is 2.25 versus 3.08 of NSC12-C1 and the former is shorter with a thicker gold layer showing larger k

Table 2.1. Physical dimensions and properties of three different tested tipless microcantilevers.

Cantilever	Dimensions				Physical properties				Manufacturer
	L (μm)	b (μm)	h (μm)	L/b	Material	ρ (kgm^{-3})	$k^{\dagger}$ (Nm^{-1})	f_{air} (kHz)	
TL-NCH1	124	42	4.7	2.95	Si	2320	79.9	381.9	Nanosensors Inc.
NSC12-B	81	36	2	2.25	Si	2320	22.9	256.5	MikroMasch Inc.
			0.015		Cr	7140			(The Cr-Au layers were coated at the University of Tennessee)
			0.4		Au	19300			
NSC12-C1	120	39	2	3.08	Si	2320	6.87	151.3	MikroMasch Inc.
			0.015		Cr	7140			(The Cr-Au layers were coated at the University of Tennessee)
			0.1		Au	19300			

†Spring constants are calculated for a given temperature using the Sader's method and the listed numbers represent the reference spring constants calculated at T_o = 20 °C

while the relatively longer latter one with a thinner gold layer showing smaller *k* value. For each microcantilever, the spring constant is calibrated from the Sader's method [49] using the cantilever planar dimensions, the resonance frequency and *Q*-factor measured in the air.

The tested microcantilevers are mounted on the solution-compatible cantilever holder attached to the head unit of the MFP-3D-BIO™ AFM (Asylum Research Inc., Santa Barbara, CA). In order to provide a uniform temperature environment, a fluid cell of 24 mm diameter and 5 mm deep is machined on the top surface of a 85 × 50 mm copper block. The copper block contains built-in serpentine coolant passages extending to and from a temperature-controllable thermal bath (Model 1156D, VWR International Inc., West Chester, PA). A Type T thermocouple probe (better than ±0.1 °C readout uncertainty) is placed next to the cantilever to monitor the surrounding liquid temperature. Once a steady thermal environment is ensured, measurements are made for the thermal noise spectrum, the peak resonance response frequency, and the quality factor of each cantilever.

Second, well-controlled thermal experiments were performed to systematically investigate the temperature effects on the frequency response of a microcantilever immersed in aqueous medium near a solid surface (distance between a microcantilever and a solid surface is smaller than the width of a microcantilever). A moderate range of temperatures, from 30 to 70 °C, is tested to observe changes in both inertial and viscous dissipative effects of hydrodynamic loading in liquid.

Experiments are conducted to measure the flexural vibration frequency response

for microcantilevers immersed in de-ionized water near a glass substrate surface. Three different tipless silicon microcantilevers are selected for testing, and their physical layouts, material properties, and fundamental resonance frequencies in air at 20 °C are summarized in Table 2.2. The plan view dimensions (Length *L* and width *b*) are measured using a calibrated optical microscope by the author. The manufacturers provided the thicknesses (*h*) data showing 20% variations from the nominal value for TL-NCH2 and 15% variations for NSC12 series microcantilevers. TL-NCH2 is a short single-layered cantilever with the highest fundamental resonance frequency among the three. NSC12-C2 is a double side-coated cantilever with 20-nm-thick chromium and 30-nm-thick gold layers. Finally, NSC12-F is a long single-layered cantilever. All three cantilevers are intentionally selected to have approximately the same cantilever widths. For each cantilever, the spring constant is calibrated from Sader's method [49]. The tested microcantilevers are mounted on the solution-compatible cantilever holder attached to the head unit of the MFP-3D-BIO™ model AFM (Asylum Research Inc., Santa Barbara, CA). In order to provide a uniform temperature environment, a closed fluid cell is used with the BioHeater™ System (also manufactured by Asylum Research Inc.) providing uniformity within ±0.1 °C. Measurements are made for the thermal noise spectrum, the peak resonance response frequency, and the quality factor of each cantilever at a specified distance between cantilever and glass substrate surface. Separation distance up to 15 μm is controlled by force spectroscopy function of MFP-3D-BIO™ AFM with accuracy ± 0.1 μm.

Table 2.2. Physical dimensions and properties of three different tested tipless microcantilevers.

Cantilever	Dimensions				Physical properties				Manufacturer
	L (μm)	b (μm)	h (μm)	h/L^2 (m^{-1})	Material	ρ_c (kgm^{-3})	$k^{\dagger}$ (Nm^{-1})	f_{air} (kHz)	
TL-NCH2	125	39.2	4.3	275	Si	2320	58.6	352.6	Nanosensors Inc.
NSC12-C2	122	33	2	141	Si	2320	6.47	165.4	MikroMasch Inc.
			0.02		Cr	7140			
			0.03		Au	19300			
NSC12-F	240	34.4	2	34.7	Si	2320	0.63	40.95	MikroMasch Inc.

†Spring constants are calculated for a given temperature using Sader's method, and the listed numbers represent the reference spring constants calculated at T_o = 20 °C

2.4 Results and Discussion

Figure 2.1 shows predictions (Figs. 2.1-a and b) from the extended Sader's viscous model and experimental verifications (Figs. 2.1-c and d) for the case of NSC12-C1 cantilever immersed in de-ionized water. Although not shown, the corresponding results for the two remaining cantilevers are found qualitatively similar to those of NSC12-C1.

Figure 2.1-a shows the peak resonance response frequency shifts from the resonance frequency taken at the lowest 10 °C with increasing temperature. The net frequency shifts $\Delta f = \Delta f_\eta + \Delta f_\rho + \Delta f_E$ with the individual contributions due to the liquid viscosity Δf_η, to the liquid density Δf_ρ, and to the Young's modulus of cantilever Δf_E. The dissipative effect due to the liquid viscosity, Δf_η, is the dominating factor for the net frequency shifts of the entire range of tested temperatures. The inertial effect due to the liquid density, Δf_ρ, gradually increases with temperature, but its maximum at 70 °C (or ΔT = 60 °C) is approximately 15% of the net shift. For relatively larger cantilevers with few millimeter length scales, the inertial effect of the liquid is known to dominate in determining the resonance frequency shifts [50]. For the present microscale cantilevers, however, it is shown that the dissipative effect dominates in determining the resonance frequency shifts. The frequency shifts due to the Young's modulus changes, Δf_E, are negative because the cantilever stiffness decreases with increasing temperature. However, the effect is minimal compared to the previous two effects.

Figures 2.1-b and 2.1-c, respectively, show the predicted and measured power spectral density (PSD) distributions of the slope of the cantilever immersed in de-ionized

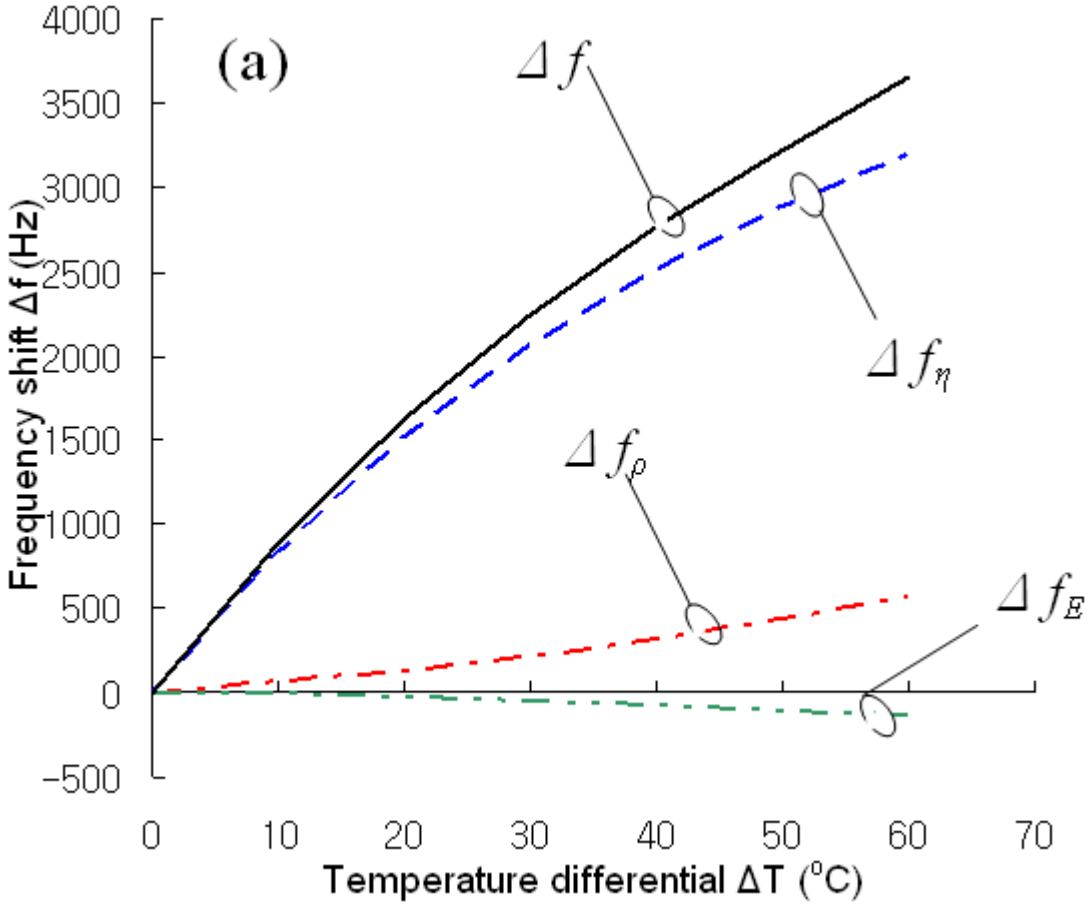

Figure 2.1-a: Theoretical predictions and experimental verifications of the thermally induced resonance frequency spectra and the *Q*-factor for NSC12-C1 cantilever immersed in de-ionized water: (a) Predictions based on the extended Sader's viscous model for individual contributions to the net peak resonance response frequency shifts ($\Delta f = \Delta f_\eta + \Delta f_\rho + \Delta f_E$) from the lower-end frequency at 10 °C due to the decrease in the liquid viscosity, Δf_η, the decrease in the liquid density, Δf_ρ, and the slight decrease of Young's modulus of cantilever, Δf_E, with increasing liquid temperature

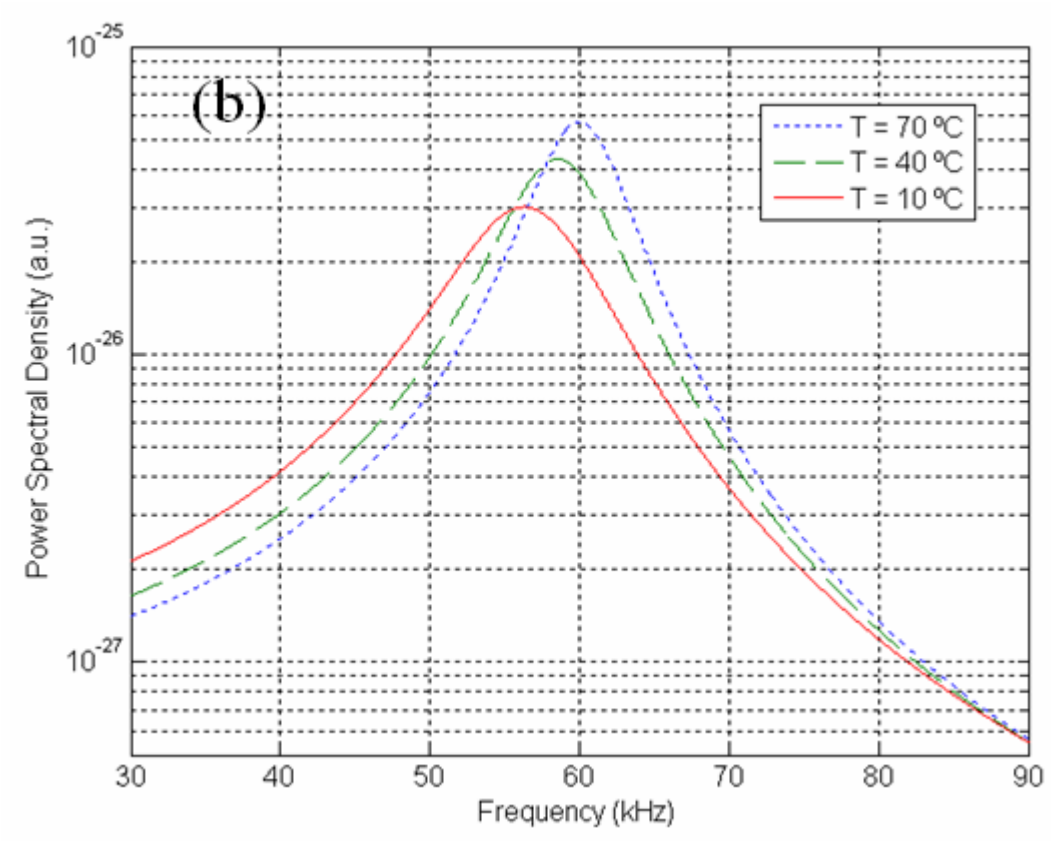

Figure 2.1-b: Continued. (b) Calculated power spectral density (PSD) of the slope of the cantilever immersed in de-ionized water at three selected temperatures of 10, 40 and 70 °C

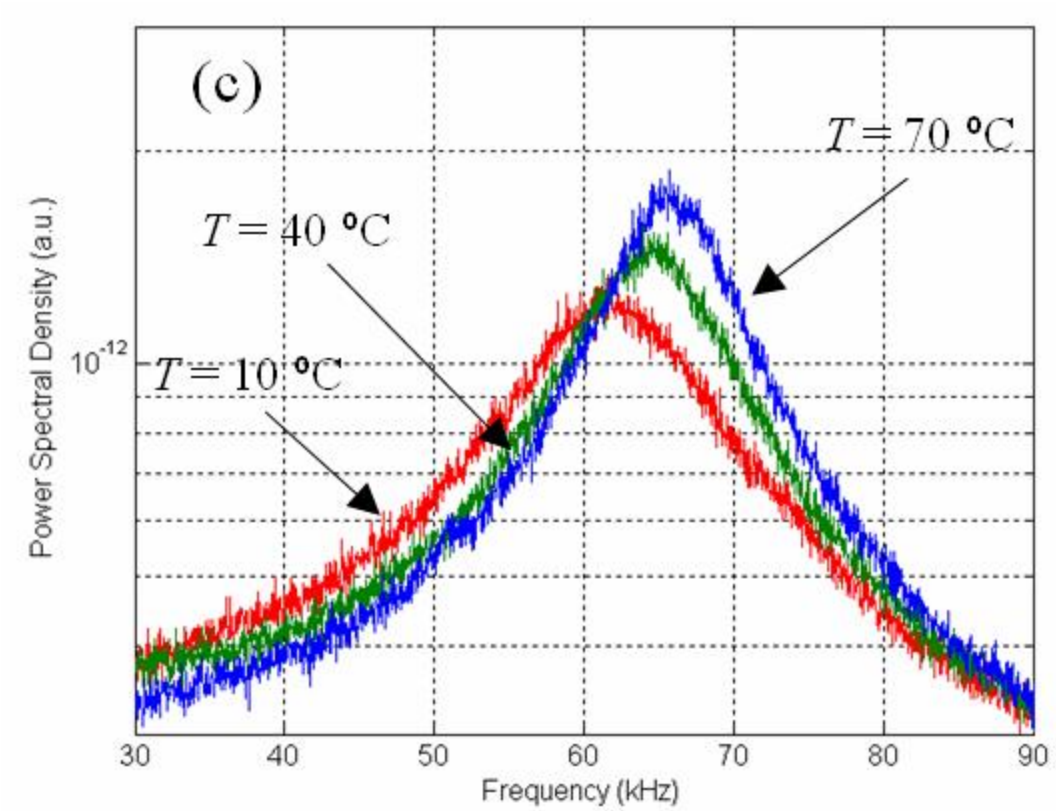

Figure 2.1-c: Continued. (c) Measured power spectral density (PSD) of the slope of the cantilever immersed in de-ionized water at three selected temperatures of 10, 40 and 70 °C

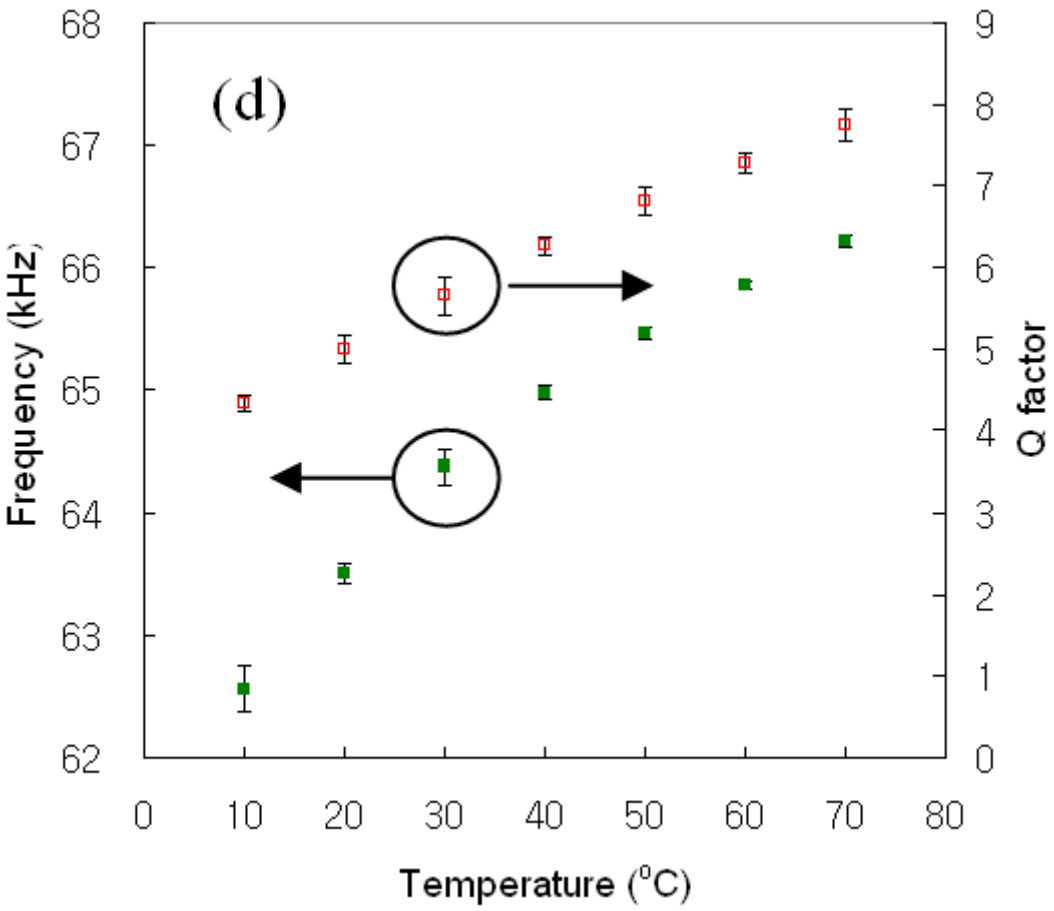

Figure 2.1-d: Continued. (d) Measured peak resonance response frequencies and the corresponding *Q*-factors at temperatures ranging from 10 to 70 °C. The error bars indicate 95% confidence intervals of measured data.

water at three selected temperature conditions: 10, 40 and 70 °C. The calculated peak resonance response frequencies are approximately 10% underestimation from the measured values, for all three temperatures. Additionally, the findings from the other two cantilevers displayed similar results, which is in accordance with the Sader's original findings where the models were derived for an infinite aspect ratio (*AR*). In practice, cantilevers with finite *AR*'s are expected to have higher resonance frequencies.

Figure 2.1-d shows the measured peak resonance response frequencies and the *Q*-factors of the NSC12-C1 cantilever. The increase of the resonance frequency with increasing temperature verifies the dominant effects of the liquid viscosity and density as shown with predictions in Fig. 2.1-a. The higher *Q*-factor at higher temperature indicates that both dissipative and inertial effect decrease with increasing temperature. Note that the *Q*-factor shows strong dependence on liquid temperature and varies by a factor of two, approximately from 4 to 8, for the tested temperature range from 10 to 70 °C.

Figure 2.2 shows the peak resonance response frequency shifts from the lower-end frequency at 10 °C as functions of temperature for the three tested cantilevers. Each symbol represents the averaged frequency shifts from ten (10) measurements, with the error bar corresponding to 95% confidence interval. The three curves show calculated frequency shifts based on the aforementioned extended Sader's viscous model. While both the single-layered TL-NCH1 (*AR* = 2.95) and the double-layered NSC12-C1 (*AR* = 3.08) cantilevers agree with the extended Sader's viscous model and the present experimental results, the shorter and double-layered NSC12-B (*AR* = 2.25) cantilever deviates from the theory with increasing temperature. This deviation can logically be attributed to the small aspect ratio that does not constitute the basic assumption of the

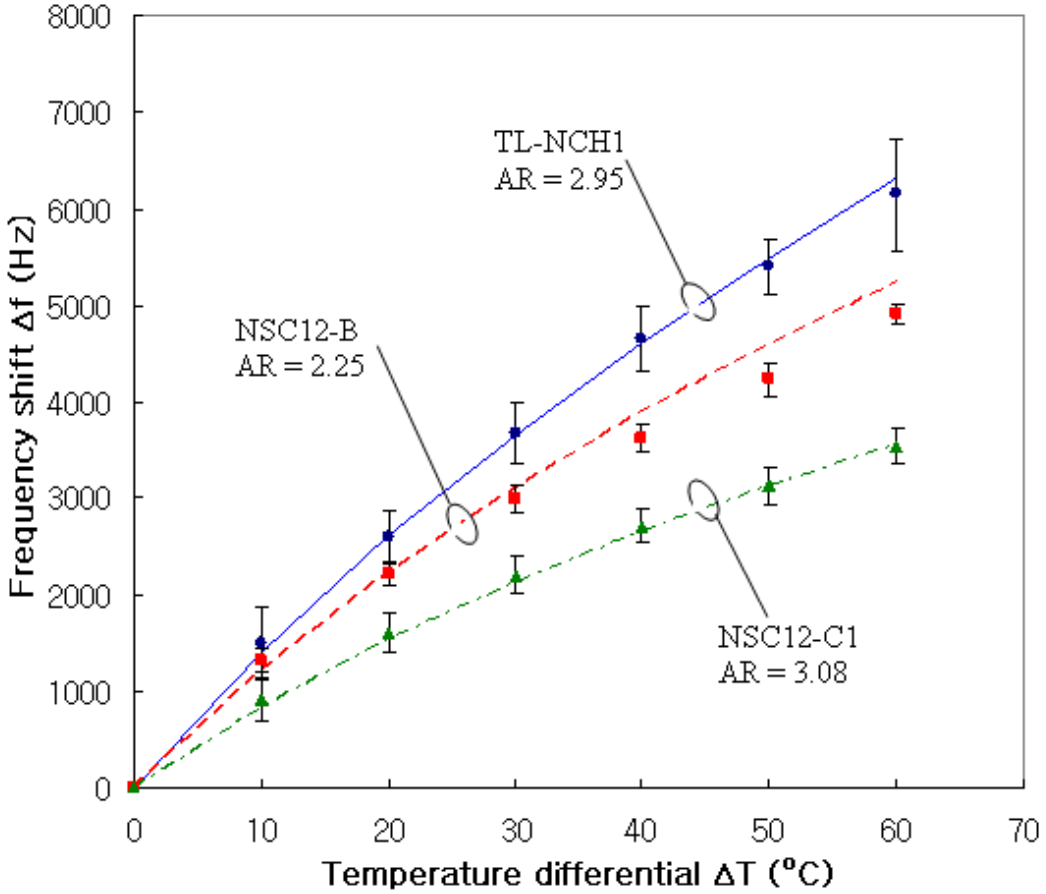

Figure 2.2: Magnitudes of the peak resonance response frequency shifts as functions of the temperature differential from the lower-end 10 °C for the three tested TL-NCH1, NSC12-B, and NSC12-C1 cantilevers. The curves represent theoretical predictions by the extended Sader's viscous model and the symbols represent the averaged shifts of the peak resonance response frequencies with the error bars showing 95% confidence intervals of measured data.

Sader's model, which basically adopts an infinite aspect ratio.

Figure 2.3 shows theoretical predictions from the extended Sader's viscous model for a microcantilever immersed in de-ionized water near a solid surface. In this case, TL-NCH2 cantilever parallel to a solid surface is assumed. The dimensionless distance parameter, H, is the ratio of the separation distance of the cantilever beam from the surface, h_0, to the width of the cantilever beam, b. With increasing temperature, for both cases of H = 0.1 and 1.0, the liquid viscosity decreases, and the magnitude of the resonant frequency increases because of the reduced viscous dissipation. At a constant temperature, the resonant frequency at H = 0.1 is lower than that of H = 1.0 because of increased viscous dissipation as the wall is approached. However, the resonance frequency shift $\Delta f^{H=0.1}$, for a given temperature differential ΔT, is much greater than the frequency shift $\Delta f^{H=1.0}$. This implies that the thermal response of the resonance frequency, namely $\Delta f / \Delta T$, is more sensitive as the cantilever approaches the wall.

The net frequency shift, $\Delta f = \Delta f_\eta + \Delta f_\rho + \Delta f_E$, consists of the individual contributions due to the liquid viscosity Δf_η, liquid density Δf_ρ, and Young's modulus of cantilever Δf_E. The dissipative effect due to the liquid viscosity Δf_η is the dominating factor in determining the net frequency shifts for both H = 0.1 and 1.0, and the dominance increases noticeably with decreasing separation distance. At 70 °C (ΔT = 40 °C), for example, $\Delta f_\eta / \Delta f$ increases from 0.73 at H = 1.0 to 0.92 at H = 0.1. Therefore, when a cantilever approaches the wall, the temperature effect represented by the viscous dissipation becomes more pronounced. This effect accounts for the more

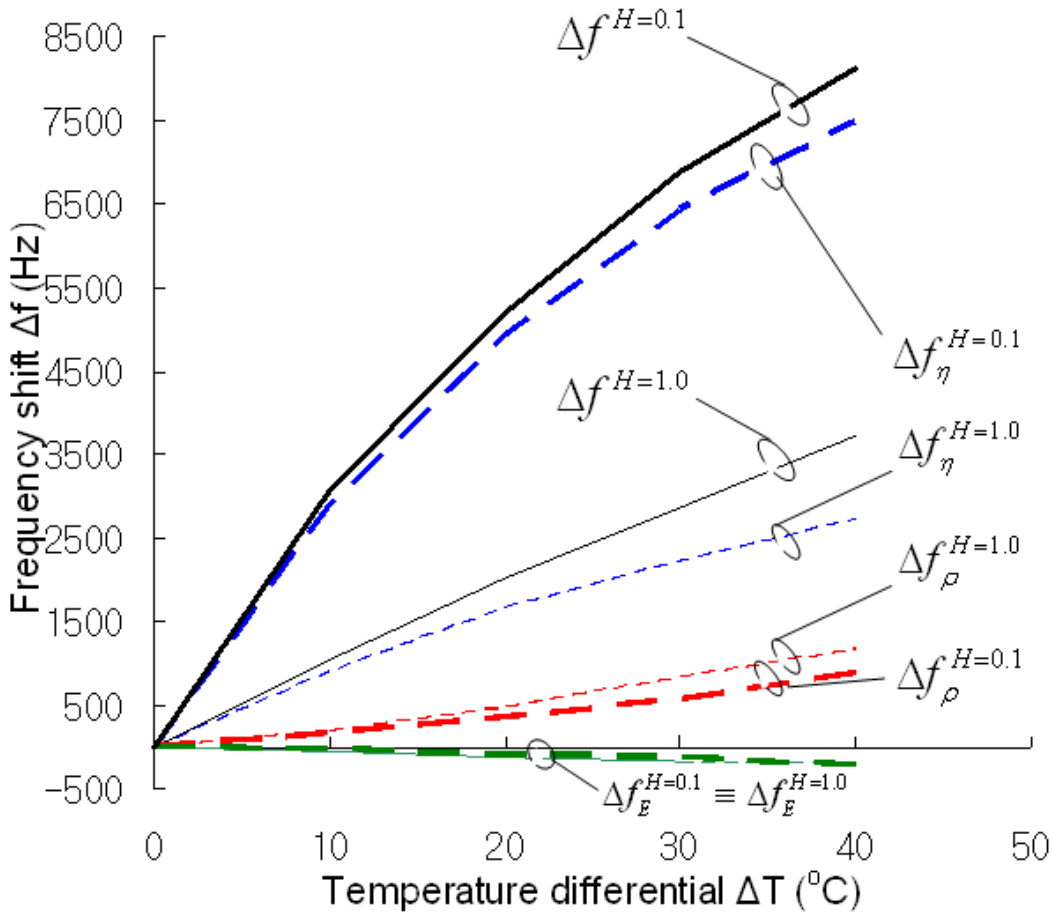

Figure 2.3: Theoretical predictions of the thermally induced resonance frequency shifts for TL-NCH2 cantilever immersed in de-ionized water near a solid surface. Predictions based on modification of Sader's model for individual contributions to the net peak resonance response frequency shifts ($\Delta f = \Delta f_{\eta} + \Delta f_{\rho} + \Delta f_{E}$), the decrease in dissipative effect by the liquid viscosity Δf_{η}, the decrease in inertial effect by the liquid density Δf_{ρ}, and the slight decrease of Young's modulus of cantilever Δf_{E}, with increasing liquid temperature at different normalized separation distances H = 0.1 and 1.0.

rapid increase in Δf for H = 0.1 than for H = 1.0.

The inertial effect due to the liquid density Δf_ρ gradually increases with temperature, but $\Delta f_\rho / \Delta f$ shows a decrease from 0.32 to 0.11 when H decreases from 1.0 to 0.1. For macroscale cantilevers with length scales of a few millimeters, the inertial effect of the liquid is known to dominate in determining the resonance frequency shifts [50]. For the present microscale cantilevers, however, it is shown that the dissipative effect dominates in determining the resonance frequency shifts. The frequency shifts due to Young's modulus changes Δf_E are negative because the cantilever stiffness decreases with increasing temperature and is unaffected by proximity to a surface. Moreover, the effect is minimal compared to the previous two effects. Although not shown, the corresponding results for the other two cantilevers (NSC12-C2 and NSC12-F) are found qualitatively similar to those of TL-NCH2.

Figure 2.4 shows the predicted and measured peak resonance response frequency shifts as functions of temperature differential from 30 °C, for the case of TL-NCH2 cantilever. The curves represent theoretical predictions by the modified Sader's viscous model, and each symbol represents the averaged frequency shifts from ten measurements, with the error bar corresponding to a 95% confidence interval. While generally enhanced thermal sensitivities ($\Delta f/\Delta T$) are observed in the near-wall region due to the additional hydrodynamic loading effects as previously discussed in association with Fig. 2.3, large discrepancies are also identified between the predictions and measurements. This is believed to be attributed to the definition of the separation distance H.

The theory assumes a parallel cantilever to the wall, but the measurements use a

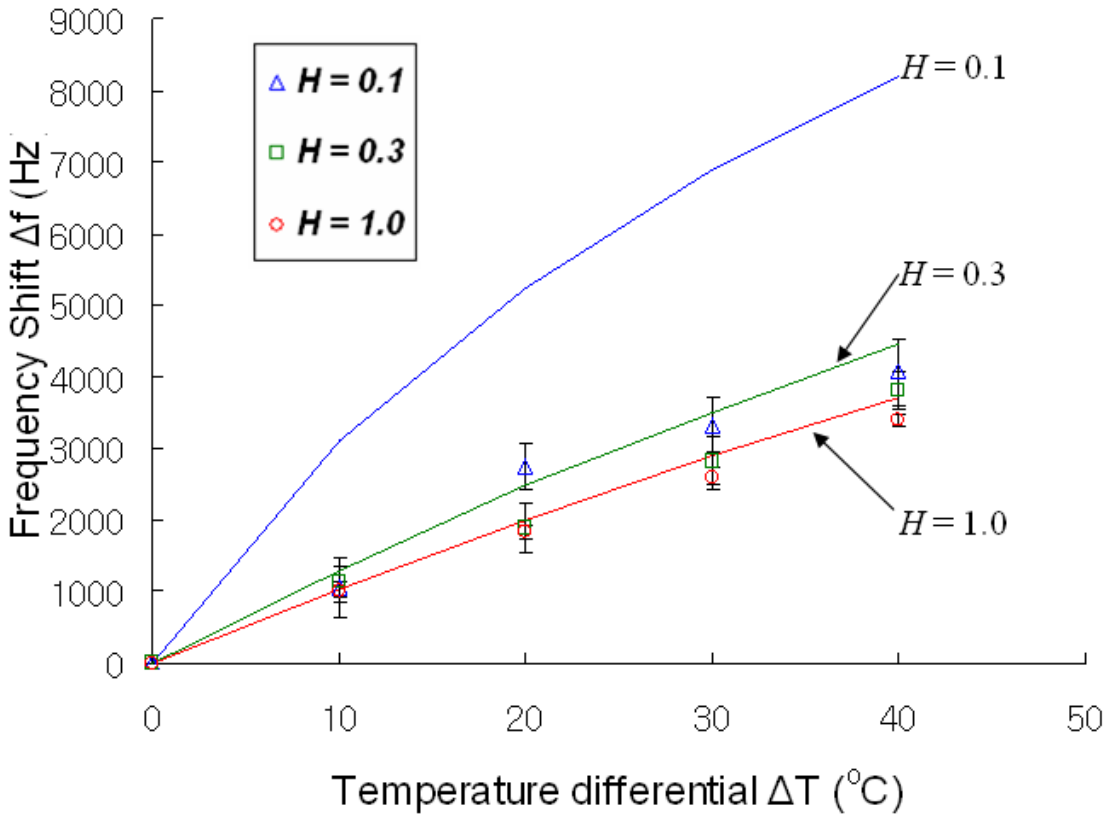

Figure 2.4: Calculated and measured peak resonance response frequency shifts from the lower-end frequency at 30 °C as functions of temperature for TL-NCH2 cantilever immersed in de-ionized water at different separation distances. The curves represent theoretical predictions by the modified Sader's model, and the symbols represent the averaged shifts of the peak resonance response frequencies with the error bar showing 95% confidence intervals of measured data. Note that the separation distance *H* is defined based on the tip-to-wall distance, while the practical cantilever is inclined at a small angle from the horizon.

tilted cantilever at an angle of 11° from the horizon. Nevertheless, the nominal separation distance for the tilted cantilever is defined based on the tip-to-wall distance, i.e., the shortest distance. A recently published model by Clarke et al. supports this argument and demonstrates the striking sensitivity of thermal noise spectra to the tilted cantilever angle [51]. Thus, if this extended Sader's viscous model near a solid surface is properly modified to consider the inclination of the practical cantilevers, agreement is expected to exist between the predictions and measurements.

Figure 2.5 shows calculated near-wall thermal sensitivity, $\Delta f/\Delta T$, for the case of silicon cantilevers as functions of h/L^2 for three different widths of 20, 30, and 40 μm. The fundamental resonant frequency of a microcantilever in vacuum is given as $f_{vac} = \frac{1}{2\pi}\sqrt{\frac{k}{m}} = Const\frac{h}{L^2}\sqrt{\frac{E}{\rho_c}} = f\left(\frac{h}{L^2}, \frac{E}{\rho_c}\right)$, i.e., the fundamental resonant frequency increases with increasing h/L^2 (a thicker or a shorter cantilever) as well as increasing E/ρ_c (a stiffer cantilever). I believe that these two parameters, h/L^2 and E/ρ_c, more comprehensively describe the microcantilever resonance characteristics than the conventional choice of the aspect ratio (L/b). The temperature differential is set to 40 °C according to our experimental condition, and the nominal cantilever height is set to H = 0.5. The sensitivities predicted at different heights (H), though not shown, show qualitatively similar behaviors. The thermal sensitivity increases with increasing h/L^2, which is consistent with the finding that the fundamental resonance frequency increases with h/L^2. This is attributed to the fact that, at higher resonance frequencies, the viscous dissipative loading effect is more pronounced in determining the thermal sensitivity [52].

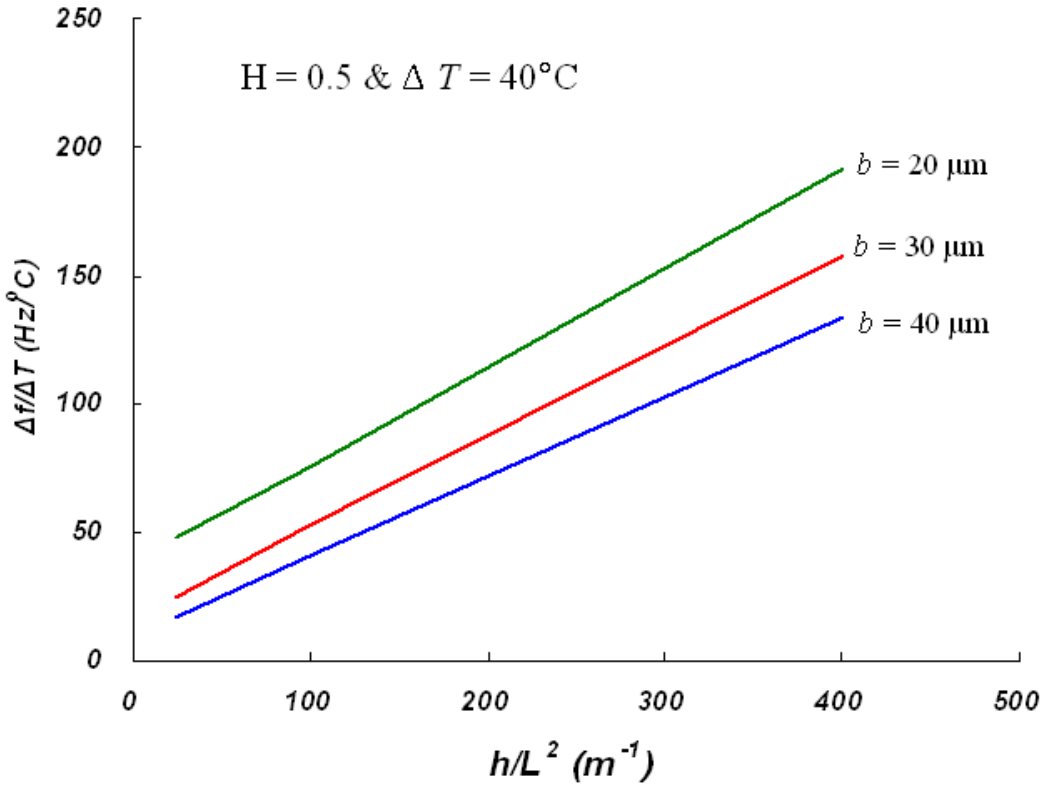

Figure 2.5: Calculated near-wall thermal sensitivity $\Delta f/\Delta T$ at H = 0.5 of microcantilevers made of silicon as functions of h/L^2 for three different widths b = 20, 30, and 40 μm.

Furthermore, once h/L^2 is fixed, the sensitivity increases with a narrower cantilever (smaller b) with a lower spring constant k, which is more susceptible to the thermal property changes of the surrounding liquid. Therefore, the cantilever sensitivity, as near-wall thermometry, increases with increasing thickness, decreasing length, and decreasing width when the cantilever material is specified.

Figure 2.6 shows the peak resonance response frequency shifts as functions of ΔT for the three tested cantilevers. Note that the widths of the three selected cantilevers are approximately the same within ±10%. Each symbol represents the averaged frequency shifts of ten (10) individual measurements, and the three types of symbols (triangles, squares, and circles) represent the data taken at H = 0.1, 0.3, and 1.0, respectively. The three curves show calculated frequency shifts for the case of H = 1.0 based on the extended Sader's viscous model near a solid surface. The cantilevers with relatively large h/L^2 and high fundamental resonance frequencies (TL-NCH2 and NSC12-C2) show distinctions in the measured frequency shifts depending on H at each specified temperature differential, while the cantilever with smaller h/L^2 (NSC12-F) shows diminished dependence on H. This is consistent with the previous findings that the near-wall viscous dissipation to temperature increase for a thicker or shorter cantilever is more pronounced in comparison with that of a thinner and longer cantilever.

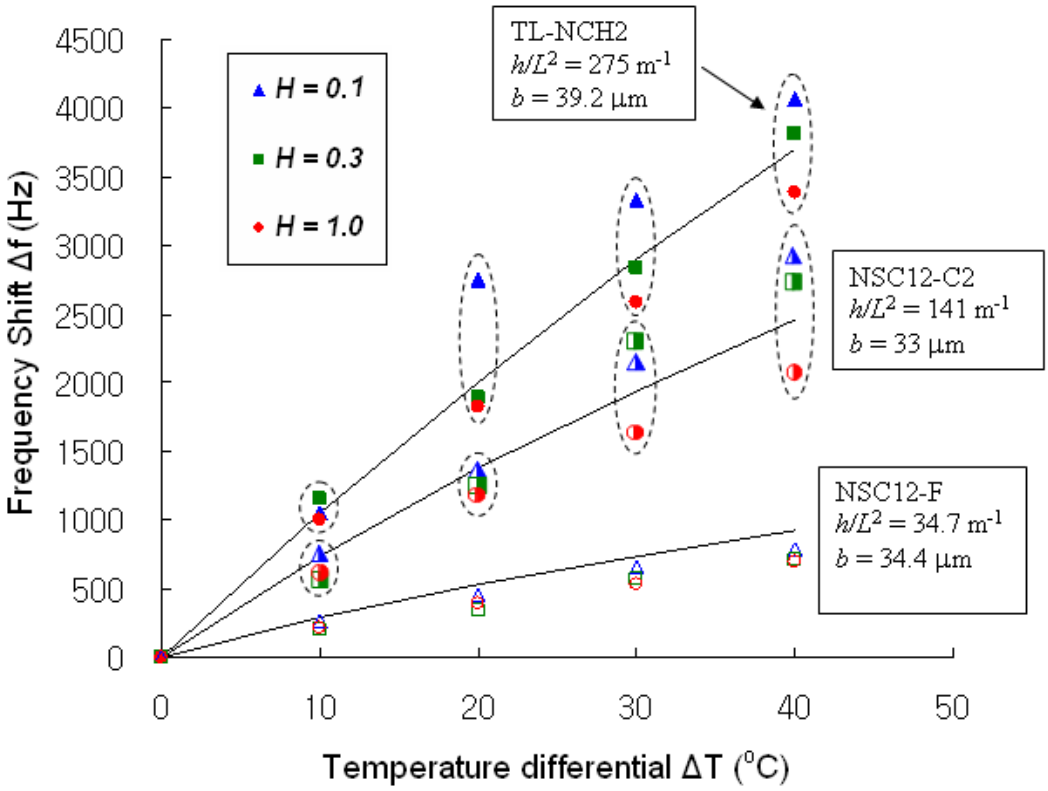

Figure 2.6: Magnitudes of the peak resonance response frequency shifts as functions of the temperature differential from the lower-end 30 °C for the three tested TL-NCH2, NSC12-C2, and NSC12-F cantilevers. The curves represent theoretical predictions at H = 1.0, and the three families of symbols (triangles, squares, and circles) represent the average shifts of the peak resonance response frequencies measured at three different separation distances H = 0.1, 0.3, and 1.0, respectively.

2.5 Conclusion

Experimental verification of the extended Sader's model has been attempted for thermally induced shifts of the peak resonance response frequencies and the *Q*-factors of three different microcantilevers immersed in de-ionized water at controlled temperatures ranging from 10 to 70 °C. The peak resonance response frequency shifts are dominated by the temperature effects associated with the viscosity and density of de-ionized water, and the effect associated with the cantilever elasticity variation with temperature is far less substantial. Measured data for both single- and multi-layered cantilevers with *ARs* of 2.95 and 3.08, respectively, agree with the extended Sader's model, while a cantilever with a smaller *AR* of 2.25 shows increasing deviations with increasing temperature.

Experimental investigation of the extended Sader's viscous model near a solid surface has been attempted for thermally induced shifts of the peak resonance response frequencies of three different microcantilevers immersed in de-ionized water near a solid surface at controlled temperatures ranging from 30 to 70 °C. The peak resonance response frequency shifts are dominated by the temperature effects associated with the viscous dissipative and inertial effect of de-ionized water, and the effect associated with the cantilever elasticity variation with temperature is far less substantial. Discrepancies of the predictions based on the extended Sader's viscous model near a solid surface, which assumes a parallel cantilever, are identified from the present measurements using inclined microcantilevers. The near-wall temperature sensitivities of the resonance frequency shifts increase with increasing h/L^2 (a thicker and shorter cantilever), increasing E/ρ_c (a stiffer cantilever), and decreasing cantilever width *b*. Therefore, shorter and thicker cantilevers made of identical materials of silicon with approximately the same width are

expected to provide higher thermal sensitivity, particularly in the near-wall region.

CHAPTER 3

Effect of adsorption-induced surface stress change on the frequency response of a microcantilever immersed in saline solution

3.1 Introduction

Microcantilevers have been utilized as biological, chemical, and physical sensor platforms for a decade. The resonance frequency shift and the deflection of a microcantilever are two main transduction mechanisms for microcantilever sensors and vary as a function of analytes adsorption [53-55]. Various sensors based on these mechanisms have been successfully developed for analytes detection in gaseous environments. In addition, many models have been proposed to explain adsorption-induced surface stress change and its resultant resonance frequency shift or deflection of a microcantilever in vacuum or in gaseous environment [56-59]. However, for liquid environments, the development of microcantilever sensors has suffered from several drawbacks, including a low quality factor, its generally narrow dynamic range, parasitic deflection, and long-term drift. Only few studies have examined the effect of adsorption-induced surface stress change on the microcantilever transduction mechanisms in liquid environment [60, 61].

The potentially extensive needs of microcantilever sensors in biological and chemical applications in liquid environments make it essential to elucidate the effect of adsorption-induced surface stress change on the resonance frequency shift of a microcantilever for correct interpretation of measured data. Although a few research groups have published quantitative experimental and theoretical results for this effect [32,

60, 61], their analysis based on simple approximate equation still needs some refinement.

3.2 Theoretical Background

Recently, Sader [39] and Green and Sader [40] presented theoretical models to predict thermally driven resonance frequencies of a microcantilever immersed in different viscous fluids. Their model was examined by the author's own experimental validation conducted at different temperatures yielding different viscosities and densities for the case of an aqueous medium [62, 63]. Indeed these previous studies showed feasibility of using a microcantilever as a thermometry tool. In order to examine the frequency response of a microcantilever as a salinity detection sensor, the adsorbed mass of ions δm and the spring constant change δk should be additionally accounted for a microcantilever with possible surface adsorption and stiffness changes.

Assuming evenly distributed adsorption of sodium and/or chloride ions on microcantilever surface, the governing equation for the dynamic deflection function $w(x,t)$ of the cantilever is modified to:

$$(EI + \delta EI)\frac{\partial^4 w(x,t)}{\partial x^4} + (\mu + \delta\mu)\frac{\partial^2 w(x,t)}{\partial t^2} = F(x,t) \tag{1}$$

where E is Young's modulus, I is the moment of inertia of the cantilever, δEI is the bending moment change of the cantilever due to adsorption-induced surface stress change, μ is the mass per unit length of the cantilever, $\delta\mu$ is the adsorbed mass of ions per unit length of the cantilever, F is the external applied force per unit length, x is the spatial coordinate along the length of the cantilever, and t is time.

Although recently the relationship between surface stress and cantilever stiffness in

vacuum is successfully established using finite element analysis [64], the origin of this bending moment change of a microcantilever in saline solution is still not well understood. While effects of surface elasticity have been proposed to explain this bending moment change, the determination of a surface elastic modulus remains elusive [65].

The fundamental resonance frequency $\omega_{vac,2}$ of a microcantilever of mass m_c in vacuum accounting for the adsorbed mass of ions δm and the spring constant change δk is given as:

$$\omega_{vac,2}(T) = \omega_{vac,1}(T)\sqrt{\frac{k+\delta k}{k}}\sqrt{\frac{m_c}{m_c+\delta m}} \tag{2}$$

where $\omega_{vac,1}$ is the fundamental resonance frequency in vacuum without mass adsorption and adsorption induced spring constant change, T is the surrounding medium temperature in which the cantilever is submerged, k is the calibrated reference spring constant with the Sader's method [49].

The adsorbed mass of sodium ions can be estimated using the Gibbs adsorption equation together with the concentration dependence of surface stress change of a gold coated silicon nitride cantilever as $d(\delta\sigma)/dC \approx 0.43 Nm^{-1}M^{-1}$ [60]. Table 3.1 shows the adsorbed mass of sodium ions δm calculated for different microcantilevers with various physical dimensions (Table 3.2).

The spring constant change δk can be iteratively determined until the predicted peak resonance response frequency shift Δf_{theo} in a specific saline concentration using Eq. (2) converges to the measured peak resonance response frequency shift Δf_{exp} under the identical conditions.

Table 3.1. The adsorbed mass of sodium ions of the four tested cantilevers for the different NaCl concentrations.

NaCl concentration C (mol/kg)	ORC8-A δm (kg)	ORC8-B δm (kg)	ORC8-C δm (kg)	ORC8-D δm (kg)
0.5	0.8×10^{-14}	1.6×10^{-14}	0.4×10^{-14}	0.8×10^{-14}
1.0	1.6×10^{-14}	3.2×10^{-14}	0.8×10^{-14}	1.6×10^{-14}
1.5	2.4×10^{-14}	4.8×10^{-14}	1.2×10^{-14}	2.4×10^{-14}
2.0	3.2×10^{-14}	6.4×10^{-14}	1.6×10^{-14}	3.2×10^{-14}

Table 3.2. Physical dimensions and properties of four different tested microcantilevers.

Cantilever	Dimensions					Physical properties				Manufacturer
	L (μm)	b (μm)	h (μm)	h/L^2	L/b	Material	ρ (kgm^{-3})	$k^{\dagger}$ (Nm^{-1})	f_{air} (kHz)	
ORC8-A	100	40	0.831	90.6	2.5	Si_3N_4	3100	0.888	76.940	Veeco Inc.
			0.015			Cr	7140			
			0.06			Au	19300			
ORC8-B	200	40	0.831	22.7	5	Si_3N_4	3100	0.143	21.772	Veeco Inc.
			0.015			Cr	7140			
			0.06			Au	19300			
ORC8-C	100	20	0.831	90.6	5	Si_3N_4	3100	0.483	80.407	Veeco Inc.
			0.015			Cr	7140			
			0.06			Au	19300			
ORC8-D	200	20	0.831	22.7	10	Si_3N_4	3100	0.075	22.333	Veeco Inc.
			0.015			Cr	7140			
			0.06			Au	19300			

†Spring constants are calculated for a given temperature using the Sader's method and the listed numbers represent the reference spring constants calculated at T_o = 25 °C

3.3 Experimental Methods

This study also presents well-controlled experiments to systematically investigate the effect of adsorption-induced surface stress change on the resonance frequency shift of a microcantilever immersed in saline solution. A wide range of sodium chloride (NaCl) concentrations up to 2.0 molality (116.88g of NaCl per kg of water) is tested to observe changes in the resonance frequency of a microcantilever.

Experiments are conducted to measure the flexural vibration frequency response for four different microcantilevers immersed in saline solution with varying salt concentrations at 25 °C. Four different rectangular silicon nitride microcantilevers with different aspect ratios (L/b = 2.5, 5, 5, and 10, respectively) are selected for testing and their physical layouts, material properties, and fundamental resonance frequencies in air at 25 °C are shown in Table 3.2. The thicknesses of microcantilevers are measured using a scanning electron microscope. The manufacturers provided the coating thicknesses data. For each cantilever, the reference spring constant is calibrated from the Sader's method. The tested microcantilevers are mounted on the solution-compatible cantilever holder attached to the head unit of the MFP-3D-BIO™ AFM (Asylum Research Inc., Santa Barbara, CA). In order to provide a uniform temperature environment, a closed fluid cell is used with the BioHeater™ System (also manufactured by Asylum Research Inc.) providing uniformity within ±0.1 °C. Measurements are made for the thermal noise spectrum, the peak resonance response frequency, and the quality factor of each cantilever.

3.4 Results and Discussion

Figure 3.1 shows the peak resonance response frequency shifts from the reference frequency in de-ionized water as functions of NaCl concentration for the four tested cantilevers. Each symbol represents the averaged frequency shifts from ten (10) measurements, with the error bar corresponding to 95% confidence interval. The four curves show calculated frequency shifts based on the Sader's viscous model that assumes both δk and δm are zero. Although not shown, the resonance frequency shifts of each cantilever with and without the adsorbed mass of sodium ions δm from the reference frequency in de-ionized water are found virtually same. Thus the deviation between the experimental and theoretical frequency shifts must be mainly due to the spring constant change δk as the adsorbed mass of ions is negligibly small.

The spring constant change δk in different NaCl concentrations are determined with experimental fitting as described previously and the results are shown in Table 3.3. The tested cantilevers tend to be stiffer with increasing NaCl concentration and maximum percentile change of spring constant is 1.47% increase from the reference spring constant. This stiffening trend of cantilevers is attributed to the electrostatic repulsive interaction between the adsorbate ions which increases total surface stress and bending moment.

Figure 3.2 shows measured NaCl concentration detection sensitivity, $\Delta f/\Delta C$, in symbols for the four tested cantilevers as functions of h/L^2 and predictions in curves assuming both δk and δm to be zero. The detection sensitivity increases with increasing h/L^2, which is consistent with our previous finding [63] that the fundamental resonance frequency increases with h/L^2. This is attributed to the fact that, at higher resonant

frequencies, the viscous dissipative loading effect is more pronounced in determining the

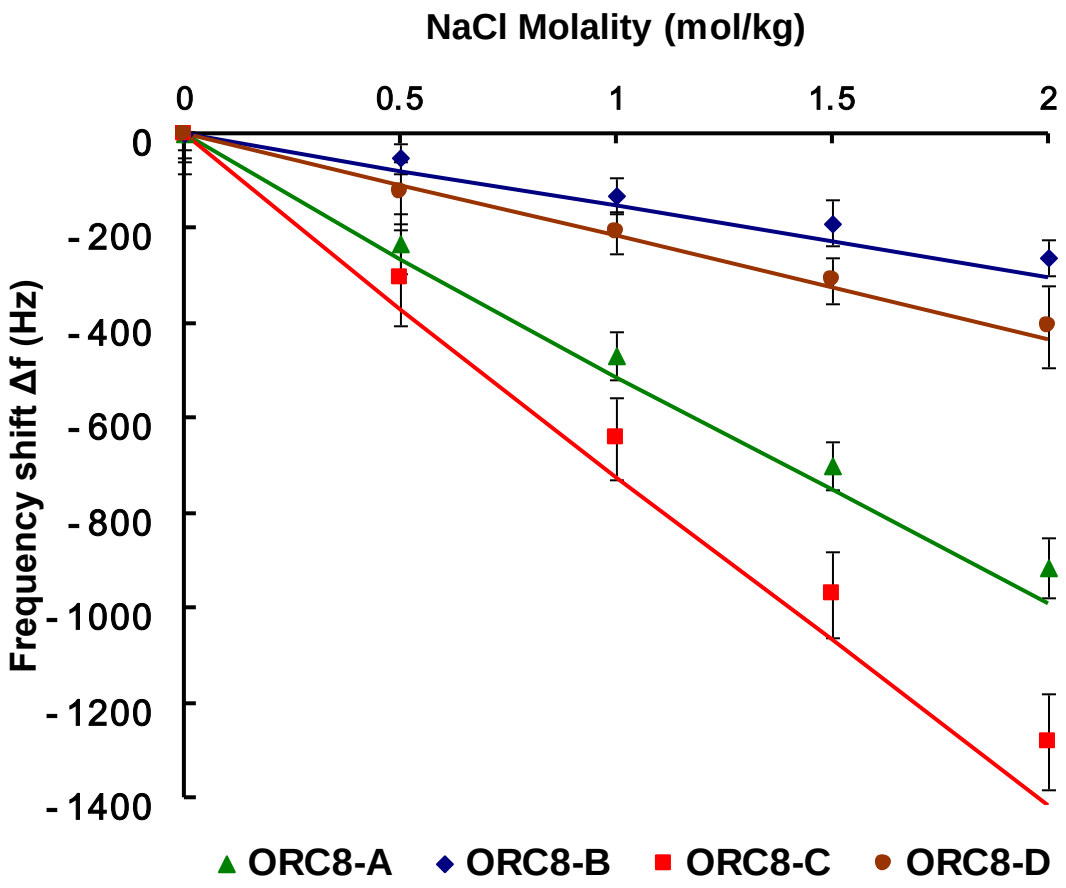

Figure 3.1: Theoretical predictions and experimental measurements of the resonance frequency shifts in saline solution from the reference frequency in de-ionized water as functions of NaCl concentration for the four tested cantilevers. The four curves show calculated frequency shifts by the Sader's viscous model assuming both δk and δm are zero and each symbol represents the averaged frequency shifts from ten (10) measurements, with the error bar corresponding to 95% confidence interval of measured data.

Table 3.3. The spring constant changes of the tested microcantilevers for the different NaCl concentrations.

NaCl concentration C (mol/kg)	ORC8-A δk (Nm^{-1})	ORC8-B δk (Nm^{-1})	ORC8-C δk (Nm^{-1})	ORC8-D δk (Nm^{-1})
0.5	2.7×10^{-3}	1.4×10^{-3}	2.1×10^{-3}	-0.3×10^{-3}
1.0	3.2×10^{-3}	1.1×10^{-3}	2.4×10^{-3}	0.2×10^{-3}
1.5	3.8×10^{-3}	1.9×10^{-3}	3.0×10^{-3}	0.3×10^{-3}
2.0	2.5×10^{-3}	2.1×10^{-3}	4.3×10^{-3}	0.6×10^{-3}

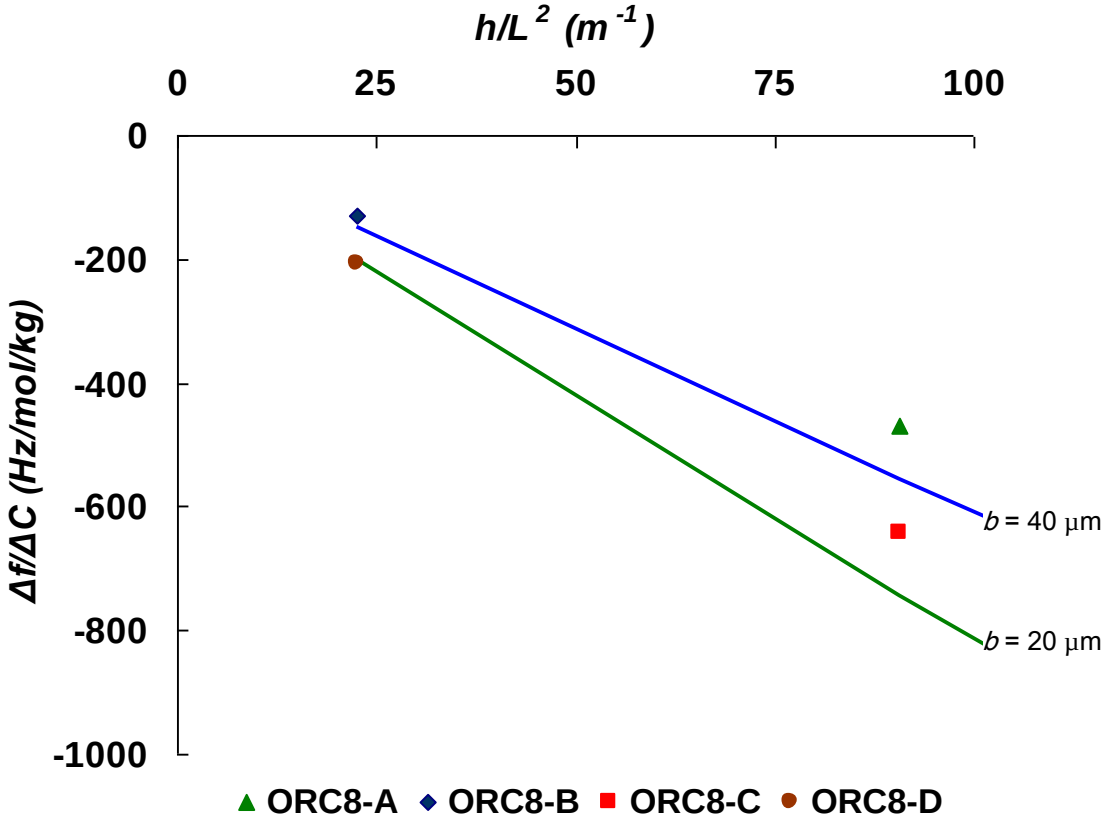

Figure 3.2: Measured and predicted NaCl concentration detection sensitivity, $\Delta f/\Delta C$, for the four tested cantilevers as functions of h/L^2 assuming both δk and δm are zero in theoretical calculation.

resonance frequency in liquid. Furthermore, once h/L^2 is fixed, the sensitivity increases with a narrower cantilever (smaller b) with a lower spring constant k, which is more susceptible to the hydrodynamic property changes of the surrounding liquid. Therefore, the cantilever sensitivity, as a salinity detection sensor, increases with increasing thickness, decreasing length, and decreasing width when the cantilever material is specified. However, we should note that the stiffening of a microcantilever in saline solution diminishes the absolute value of sensitivity and causes deviation between measurement and theoretical prediction.

3.5 Conclusion

Theoretical modification of the governing equation for the dynamic deflection function of the cantilever in saline solution as a salinity detection sensor has been attempted to accommodate the adsorbed mass and the spring constant change of a microcantilever resulting from the effect of adsorption-induced surface stress change. In addition to the hydrodynamic loadings associated with the viscosity and density change of saline solution, the spring constant change due to adsorption-induced surface stress change also influences the resonance frequency shifts and the effect associated with the adsorbed mass of ions is negligible. We determine the spring constant changes of our four different microcantilevers in saline solution with our model and measured experimental data, and identify the stiffness of our microcantilevers in saline solution tends to increase with increasing salt concentration and the absolute value of concentration detection sensitivity of our microcantilevers decreases due to the stiffening of cantilevers.

.

CHAPTER 4

Scanning thermal microscopy (SThM) technique in liquid medium

4.1 Introduction

Various approaches to micro- and nano-scale thermometry techniques have been tried for over a decade as researchers have attempted to explore the limits of spatial and temporal measurement resolution. Among them, scanning thermal microscopy (SThM) using a microfabricated thermocouple probe tip seems to be the best for achieving submicron spatial measurement resolutions for the case of solid surfaces exposed in ambient air environments [66-70]. In the case of aqueous media, however, the SThM probe has not been reported to be successful to date. Only recently, one research group demonstrated the potential of SThM as a thermometry tool in an aqueous medium but was not able to show any real temperature measurement data, which would be necessary to validate the probe's accuracy and resolutions capability [71]. Another group tried to measure cellular thermal responses in a culture medium with micro-thermocouple probe built on a glass micropipette, but no meaningful temperature signal was obtained [72].

On the other hand, several nonintrusive optical techniques have been developed to measure microscale temperature distribution in aqueous medium. The ratiometric laser-induced fluorescence (LIF) technique using fluorescent dye molecules achieved microscale spatial measurement resolution, but the measurement uncertainties were excessive particularly in the near-wall or near-meniscus region because of the interfacial interference of the fluorescent emission light [73]. Similarly, the optical serial sectioning

microscopy (OSSM) technique showed good potential as a microscale thermometry system for nanoparticle suspension fluids, but suffered from large measurement uncertainty [74]. In addition to the excessive measurement uncertainties of these optical thermometry techniques, the presence of dye molecules or dye-coated nanospheres may alter the thermal characteristics of an aqueous medium. To lessen these shortcomings that are associated with the foreign trace particles, a label-free, real-time, full-field surface plasmon resonance (SPR) reflectance sensing technique has been exploited to map microscale temperature distribution in the aqueous medium [75]. However, the detection range of this technique is confined in the near-wall region to less than 1-μm from the solid surface, thus it is hard to extend the measurement field out of the near-wall region.

Here I describe a near-field microscale thermometry sensor in an aqueous medium using a tipless microcantilever. The peak resonance response frequency and the quality factor of a microcantilever are two important dynamic characteristics that are extremely sensitive to the density and viscosity of the surrounding fluid and to the proximity of the cantilever to the solid surface [34]. Thus, these dynamic characteristics of microcantilever vibration can be calibrated to yield quantitative measurements for the fluid properties at a certain separation distance between a solid surface and a microcantilever [50]. I have verified that the dissipative effect due to liquid viscosity is the dominating factor for the resonance frequency shifts of a microcantilever. In my previous publication, I successfully correlated temperature effects on liquid properties with the thermal resonance of a microcantilever in aqueous medium in the region away from a solid surface where the no-slip wall effect is negligible [62]. Then I investigated the temperature dependence of the near-wall vibration of microcantilevers that suffer

interference from the presence of the nearby solid wall. I successfully demonstrated the concept of near-wall corrected scanning thermal microscopy working in aqueous medium [63]. However, for the concept to be more valuable as a working thermometry sensor, it will be necessary to validate the concept by experimental measurements of specified temperature fields and comparison of the data with known predictions.

This study presents well-controlled thermal experiments that validate the concept of scanning thermal microscopy (SThM) working as a near-field microscale thermometry sensor in an aqueous medium by measuring microscale temperature distributions.

4.2 Methods and Materials

In my previous study [63], I tested the near-wall thermal sensitivities of various cantilever geometries and found that the TL-NCH cantilever (length L = 135 μm, width b = 39 μm, and thickness h = 4.5 μm, Nanosensors Inc.) showed the highest near-wall thermal sensitivities among those tested. The selected microcantilever was mounted on a solution-compatible cantilever holder attached to the head unit of the MFP-3D-BIO AFM (Asylum Research Inc.) and calibrated at four specified separation distances z = 5, 10, 20, and 40 μm, which are measured between the lower end of the cantilever and the glass substrate surface. The experiments were carried out with the BioHeater™ system (Asylum Research Inc.) providing a uniform fluid temperature environment within ±0.1 °C in a steady state. Figure 4.1 shows the first peak resonance response frequencies of the TL-NCH cantilever immersed in de-ionized water as functions of specified temperatures at different separation distances. The inset schematic illustrates the experiment setup using the BioHeater™ system. Each symbol represents the averaged

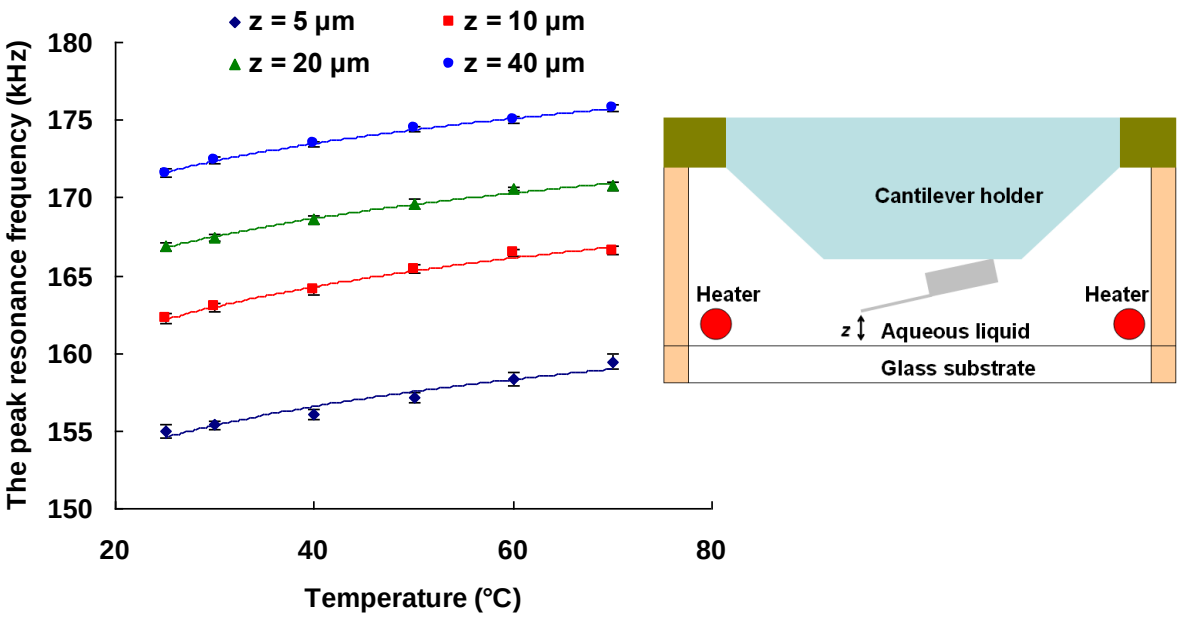

Figure 4.1: Experimental near-wall correlation of the microcantilever peak resonance response frequency with aqueous medium temperature at four different separation distances (z = 5, 10, 20, and 40 μm) between the lower end of the cantilever and the glass substrate surface.

resonance frequencies from ten measurements with the error bar of a 95% confidence interval. The cantilever vibration frequencies, quenched due to the nearby no-slip solid wall interference, should be taken into consideration in order to correlate the measured resonance frequency to the aqueous medium temperature. The corresponding power-fitting curves fairly well correlate with the measured data.

To validate the accuracy of the thermometry, a carefully designed experiment was performed to measure steady-state temperature fields in a controlled microscale thermal environment. Figure 4.2 shows the schematic of a microscale line heater working also as a temperature sensor based on the resistance-temperature relation of a thin gold film [76]. The micro-line heater consists of a vapor-deposited gold line which is 38 mm long, 100 μm wide, and 0.5 μm thick and two 3-mm-square and 0.5 μm-thick soldering pads (Fig. 4.2-a). A 500-nm-thick gold layer is deposited with a 10-nm-thick chromium adhesion layer by e-beam evaporation on the Borofloat glass substrate. The microheater patterns are deposited on the glass substrate by a lift-off technique. To physically protect and electrically insulate the micro-line heater, the top layer is coated with SU8-2002 (MicroChem Inc.) except for the soldering pads. The coating thickness is uniform at 2 μm; a 1.5 μm coating on top of the 0.5 μm heater line (Fig. 4.2-b). A feedback circuit based on the constant-temperature hot wire anemometer [77-79] is connected to provide a control for the microheater power for a constant temperature environment.

Figure 4.3 illustrates the near-field micro-thermometry sensor working for both the near-field and far-field regions in the aqueous medium. The near–field corresponds to the region that is one cantilever width from the solid interface, where the no-slip hydrodynamic boundary conditions effectively quench the thermal vibration frequencies

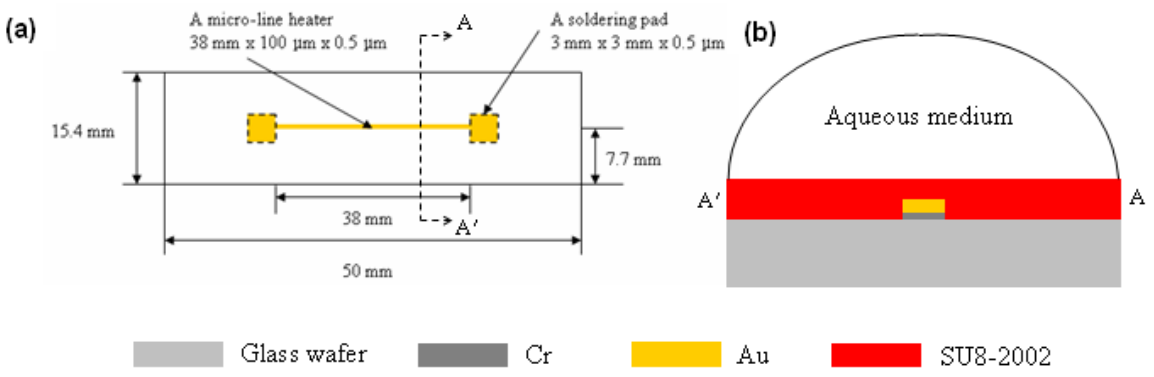

Figure 4.2: (a) A micro-line heater design. (b) Schematic illustration of the microscale thermal environment with a microheater.

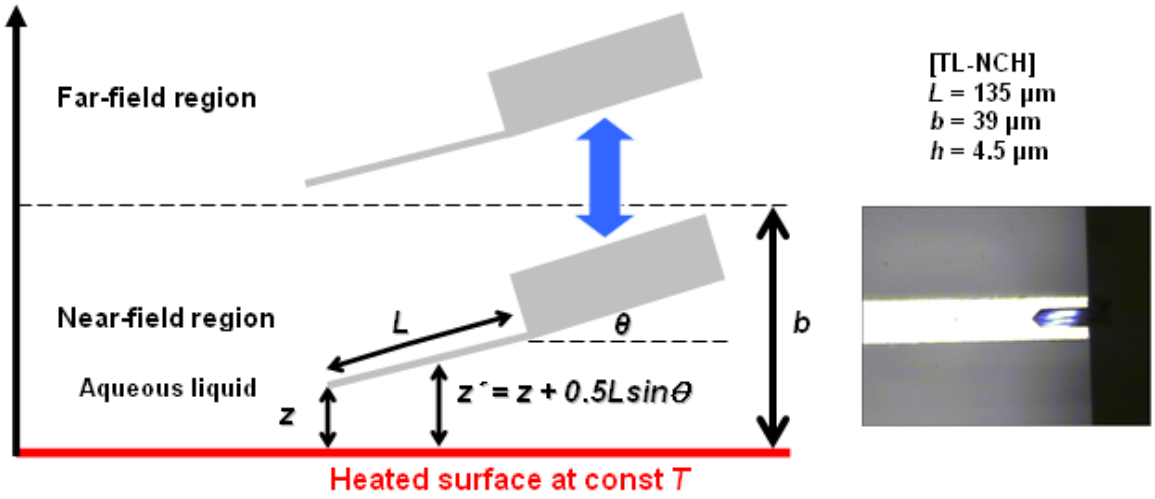

Figure 4.3: A schematic drawing of the near-field microscale thermometry in aqueous liquid using a tipless microcantilever and a microphotograph of the micro-line heater and cantilever.

of the microcantilever. Far-field thermometry has been extensively examined by means of the experimental validation in my previous publication [62], and thus the present study focuses only on the near-field thermometry. The inset photograph shows the TL-NCH cantilever aligned parallel to the 100-μm wide gold line heater shown as a thick horizontal white line. The separation distance z is controlled with 100-nm resolution by the piezoelectric actuator attached to the AFM head. The peak resonance response frequencies are measured and the data are reduced by the use of a thermal frequency fitting function, available from the MFP-3D-BIO AFM data acquisition software.

It is essential that a microcantilever of AFM be aligned at a small angle of inclination to the horizon for efficient and effective surface imaging and detection purposes. The present cantilever has an inclination angle θ of 11° and the probing site is widened to $L\sin\theta$. Assuming a linear temperature variation along the probing site, the modified separation distance $z' = z + 0.5L\sin\theta$ is taken to the midpoint of the cantilever. Note that the modified distance z' is used to calculate the temperature distributions while the nominal separation distance z is measured from the lower end of the cantilever.

Figure 4.4 presents a calculated temperature field for the two-dimensional computational domain that is consistent with the cross-section of the test medium. This two-dimensional grid was generated with CFD-GEOM software (CFD Research Corporation) and temperature field was calculated with CFD-ACE software (CFD Research Corporation). A room temperature (20°C) is imposed for all outer boundary conditions, and a constant temperature condition (50°C) is specified for the gold heater surface. The computational domain to solve for the heat conduction/convection equation consists of the microcantilever holder (k = 1.38 W/m-K), the silicon cantilever chip

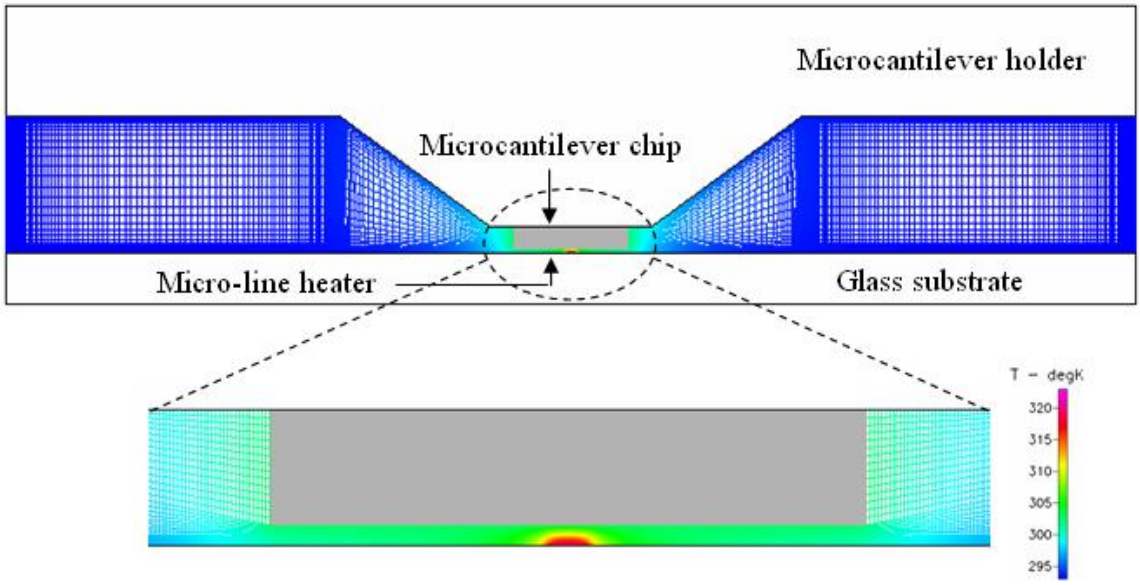

Figure 4.4: Two-dimensional computational simulation domain of the microscale thermal environment and the detailed prediction of the temperature distribution.

(k = 124 W/m-K), the aqueous medium (k = 0.613 W/m-K), SU8-2002 (k = 0.17 W/m-K), and the glass substrate (k = 1.2 W/m-K). All other thermophysical properties are assumed constant at 27°C whereas the thermophysical properties (viscosity, density, thermal conductivity, and specific heat) of water are formulated using polynomial functions of the temperature.

The temperature field shown in false color in Figure 4.4 represents the steady thermal field established in the aqueous medium over the micro-line heater when the microcantilever is separated by 40 μm from the glass substrate. The presence of the silicon microcantilever chip acts as a nontrivial heat sink because of the high thermal conductivity of silicon. Therefore, the medium temperature decreases rapidly with increasing z from the heater surface to the chip surface.

4.3 Results and Discussion

4.3.1 Transient temperature measurements

Figure 4.5 shows transient temperature measurements at z = 40 μm when the microheater temperature T_h is maintained at 50 °C, 70 °C, or 90 °C, respectively. In approximately 10 minutes after the heater is turned on, the test field temperature reaches the steady state for each of the three cases and agrees well with the corresponding calculated steady-state temperature shown by the three horizontal lines. The measured steady-state temperature remains constant for a sufficiently long period under the feedback circuit control to ensure steady thermal conditions.

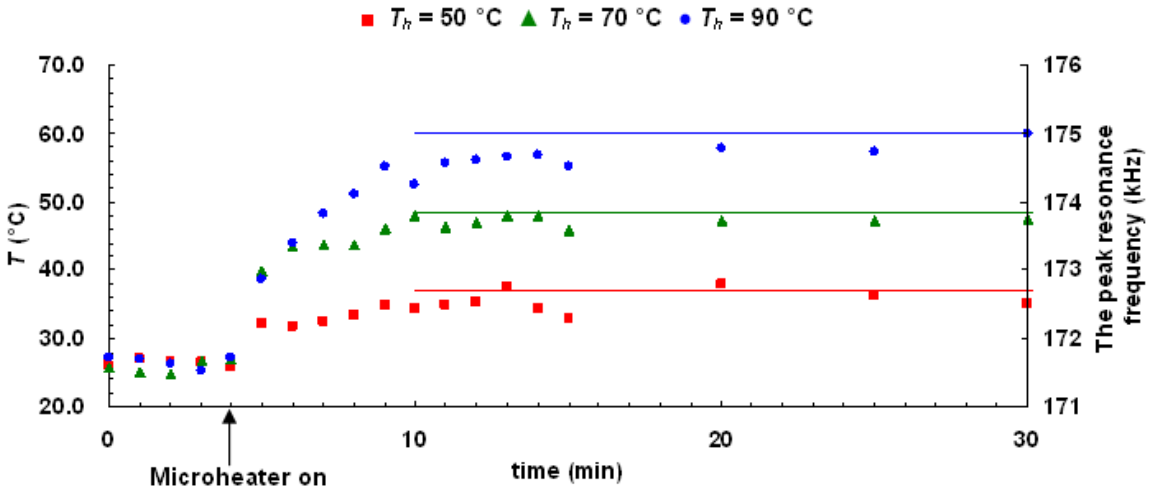

Figure 4.5: Transient temperature measurements at z = 40 µm while the microheater temperature T_h was maintained at 50 °C, 70 °C, or 90 °C.

4.3.2 Steady-state temperature measurements

Figure 4.6 shows the measured and predicted temperature profiles in the vicinity of the microheater surface at four different *z*-locations (5, 10, 20, and 40 μm) for each of three different heater temperatures (50, 70, or 90 °C). Each symbol represents the average of ten data realization measurements, and the three curves show the calculated temperature profiles based on the two-dimensional CFD calculations, accounting for the modified separation distance (z'). The measurements correlate well with the predictions, implying that the modification of the separation distance is acceptable for the cantilever midpoint.

The spatial resolution of the sensor depends on the dimensions and the inclination angle of the microcantilever. By sufficiently reducing the dimensions and the inclination angle, I expect to enhance the spatial resolution by up to one or two orders of magnitude. The measurement uncertainties can be dramatically reduced by employing the so-called quality factor enhancement scheme [80]. In addition, my theoretical predictions, based on an extended Sader's viscous model [62, 63], suggest higher thermal sensitivity is achieved when the cantilever material has a positive thermal dependence of Young's modulus dE/dT and its dimensions are reduced. Both silicon and silicon nitride have a negative thermal dependence of Young's modulus in this temperature range, however, silicon dioxide has a positive thermal dependence of Young's modulus. Therefore, for highly sensitive thermal sensor, silicon dioxide cantilever is recommended. Figure 4.7 shows calculated near-field thermal sensitivity $\Delta f/\Delta T$ for the case of silicon cantilevers as functions of h/L^2 for three different widths of 20, 30, and 40 μm [63]. The temperature differential is set to 40 °C and the normalized cantilever separation distance H (z/b) is set

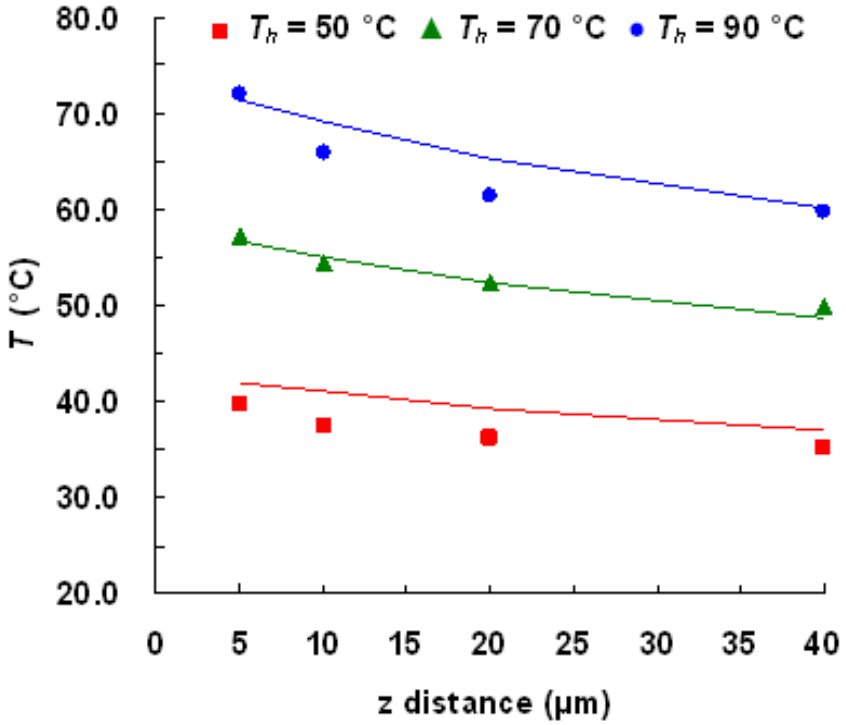

Figure 4.6: Measured and calculated steady-state temperature profiles in the vicinity of the microheater surface.

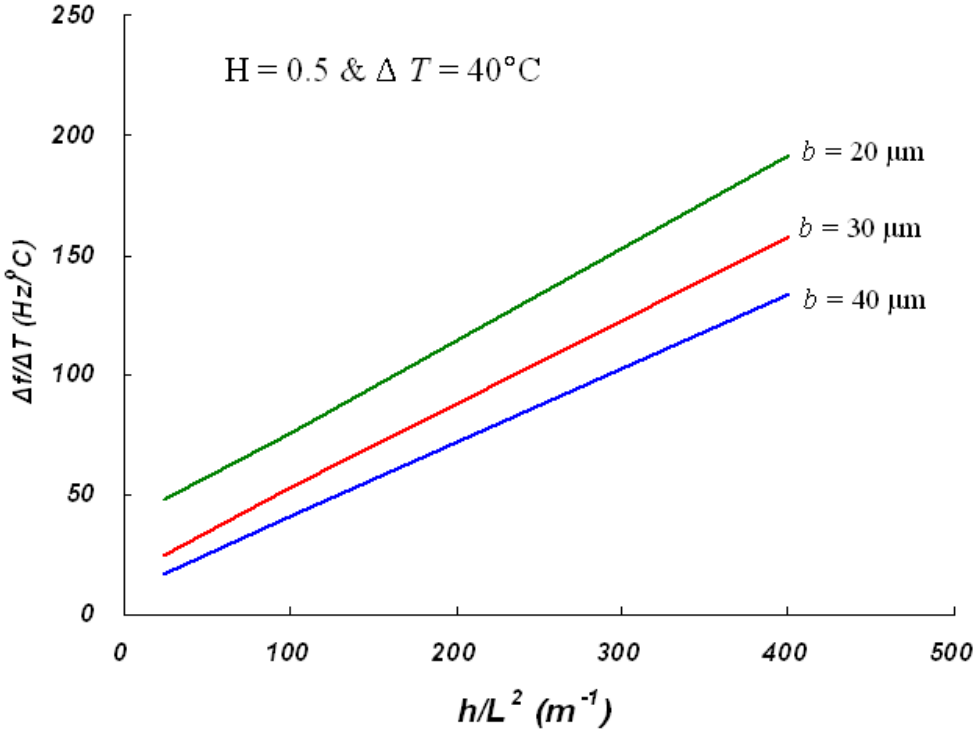

Figure 4.7: Calculated near-wall thermal sensitivity of silicon microcantilevers as functions of h/L^2 for three different widths b = 20, 30, and 40 μm [63].

to 0.5. The thermal sensitivity increases with increasing h/L^2, which is consistent with the finding that the fundamental resonance frequency increases with h/L^2. Furthermore, once h/L^2 is fixed, the sensitivity increases with a narrower cantilever (smaller b) with a lower spring constant k, which is more susceptible to the thermal property changes of the surrounding liquid. Therefore, from the theoretical point of view, the cantilever's thermal sensitivity, in its role as a near-field thermometry sensor, increases with increasing thickness, decreasing length, and decreasing width when the cantilever material is specified.

4.4 Conclusion

A new concept of a near-field thermometry sensor using a tipless microcantilever in aqueous medium is experimentally validated by conducting careful thermal field measurements. The experimental calibration, accounting for the near-wall hydrodynamic interference effect, is utilized to correlate the resonance frequency of a microcantilever with the aqueous medium's temperature. The microscale temperature measurements using this sensor agree well with the calculated predictions. To improve spatial resolution and thermal sensitivity of this sensor, use of a shorter, thicker, and narrower microcantilever is recommended based on my theoretical predictions. The microcantilever sensor can also lessen the complexity and mitigate the high cost associated with existing microfabricated thermocouples or thermoresistive sensors. It is noted that this microcantilever sensor requires relatively slow temporal resolution of an order of one second to determine the resonance frequency of a microcantilever with thermal frequency scanning, averaging, and fitting. It is expected that successful

implementation of self-excitation detection schemes to provide quasi-real time and highly accurate detection of the microcantilever resonance frequency will be essential to further develop microcantilever thermometry for real-time response to highly transient thermal fields.

CHAPTER 5

Atomic Force Spectroscopy (AFS) for the surface nanomechanical property measurements of polyelectrolyte hydrogels

5.1 Introduction

The development of atomic force microscopy (AFM) [1] and the subsequent development of atomic force spectroscopy (AFS) [15] have made it possible to probe the surface and mechanical properties of materials at a submicron scale. This is potentially significant because the surface nanomechanical properties of natural and synthetic hydrogels play a critical role in their use as biomaterials. As a result, the application of AFM technology to soft hydrogel biomaterials has a number of important applications in medicine and biomedical engineering.

Hydrogel substrate compliance has been identified as one of the key physical factors in the response of many cell types [81]. For example, both fibroblast cell locomotion and focal adhesions have been shown to be regulated by substrate compliance [82]. Aortic smooth muscle cells have been found to spread and organize their cytoskeletons and focal adhesions to a greater extent on stiff gels than on soft gels [83]. In addition, vascular smooth-muscle-cell migration has been shown to be controlled and directed by gradients in substrate compliance [84]. Further, morphotype and the expression of the focal adhesion plaque proteins of endothelial cells are also modulated by substrate elasticity [85]. Even, native mesenchymal stem cells have been shown to specify lineage and commit to phenotypes with extreme sensitivity according to substrate

elasticity [86]. Thus, the surface mechanical properties of synthetic hydrogels are emerging as an important factor in the adhesion and biological response of cells that are in contact with these materials.

The mechanical properties of synthetic hydrogels reflect the complicated combination of the neutral and charged monomer concentrations, the solvent quality, the chemical dissociation effects, and many other factors [16-21]. These competing and non-linear effects make it challenging to predict and understand the mechanical properties of these materials. In particular, the incorporation of charged monomers into an otherwise neutral and inert background has been exploited in a number of studies to promote cell adhesion and proliferation [22-25].

Atomic force microscopy is becoming an important tool for testing these complex materials, having been used both to image the surface nanotopography and to measure the surface elasticity of hydrogels in liquid solution [87-92]. The vast majority of studies that have used AFM to probe hydrogels and other biomaterials, however, have only considered isolated and random samples. By fabricating a sequence of hydrogels with systematically varying charged monomer compositions, the mechanical phase states can be more easily appreciated and understood.

This study examines the surface elasticity and charge effects on endothelial cell seeding of a sequence copolymer polyelectrolyte hydrogels. A neutral monomer, 2-hydroxyethyl methacrylate (HEMA), was copolymerized with varying proportions of the basic monomer 2-methacryloxyethyl trimethyl ammonium chloride (MAETAC). Hydrogels were prepared with increasing positive charge concentrations ranging from 0 to 400 mM. The equilibrium swelling behavior was measured as a function of the

monomer composition or the equivalently positive charge concentration, and was compared with AFM measurements of the surface elasticity. The effect of these parameters on endothelial cell attachment was demonstrated by seeding these hydrogels with porcine pulmonary artery endothelial cells (PPAECs).

5.2 Methods and Materials

5.2.1 Hydrogel preparation

A series of copolymer hydrogels, with increasing proportions of positively charged monomers, was synthesized using the neutral monomer 2-hydroxyethyl methacrylate (HEMA) and the basic monomer 2-methacryloxyethyl trimethyl ammonium chloride (MAETAC). Specifically, 1.54M HEMA (Polysciences) and 1.14 M HEMA / 0.4 M MAETAC (Polysciences) monomer stock solutions containing 40% ethylene glycol (solvent) and 20.2 mM ethyleneglycol dimethacrylate (EGDMA) (Aldrich) were initially prepared. By mixing relative proportions of the neutral HEMA and basic MAETAC stock solutions together, pregel solutions containing a total 1.54 M monomer concentration, but with MAETAC concentrations ranging from 0 to 400 mM, were prepared at 40mM increments. Stock solutions of 4 wt% initiator ammonium persulfate (APS) (Aldrich) and 15 wt% accelerator sodium metabisulfite (SMBS) (Aldrich) were also prepared. To start the polymerization reaction, 200 µL of the 4 wt% APS initiator stock solutions and 200 µL of the 15 wt% SMBS accelerator stock solutions were added to 10mL of the pregel monomer mixtures. After the monomer solutions were mixed, they were filtered with a 0.2 µm filter and injected between two glass plates separated by a 400 µm Teflon spacer

and allowed to polymerize for 24 hours at room temperature. After polymerization, the copolymer hydrogel membranes were removed from their molds and allowed to equilibrate in 154mM of NaCl solutions for several days. The NaCl bath solutions were replaced everyday to ensure equilibration.

5.2.2 Hydrogel shrinking/swelling experimental measurements

After polymerization and washing, the copolymer hydrogels were cut into circular discs for use in the AFM measurements. For the measurements of hydrogel equilibrium swelling behavior measurements, the hydrogels polymerized in their molds were cut out using a cork borer with 16.46 mm inner diameter, D_0, and washed in a 154 mM NaCl solution for several days. The shrinking/swelling behavior was recorded by measuring the hydrogel disc diameters, D, using an electronic digital caliper. The relative shrinking/swelling ratio, $(D-D_0)/D_0$, was evaluated after equilibration in solution relative to the inner diameter of the borer, D_0, that was used to cut the hydrogel.

5.2.3 AFM measurements

Surface imaging and force spectroscopy measurements were performed using an MFP-3D-BIO™ AFM (Asylum Research Inc., Santa Barbara, CA). All non-contact mode surface imaging was performed with an Olympus BioLever A cantilever (Olympus, Japan) in 154 mM of NaCl solution. The scanning size was 10 µm by 10 µm. In order to provide a physiological temperature environment, a closed fluid cell was used with the BioHeater™ System (Asylum Research Inc., Santa Barbara, CA). Force spectroscopy measurments were performed with a 6 µm polystyrene microsphere affixed to a V-shaped

silicon nitride cantilever (Bioforce Nanoscience, Ames, IA), which allowed force-displacement curve measurements under indentation without puncturing the soft gel surface. The nominal spring constant of the cantilever was 0.06 N/m. All measurements were made at 37±0.1 °C.

The position-sensitive detector signal of the AFM was calibrated by taking the slope of the deflection voltage versus the *z* displacement curve measured using a reference glass substrate surface in saline solution. Ten force-displacement curve measurements at each of five different randomly selected locations were acquired with a probing speed of 2 μm/s and approach-retraction frequency in the ranging from 0.2 Hz to 1 Hz. The indentation depth, δ, was controlled in the range from 60 nm to 600 nm, by changing the trigger voltage of the force-displacement curve measurements in order to satisfy the basic assumption of the spherical Hertz model [93, 94]. It will be recalled that the slope of a force-displacement curve describes the elastic properties of a sample qualitatively. The more elastic a sample, the steeper the slope of a force-displacement curve will be. In the spherical Hertz model, the elastic modulus E is given by

$$E = \frac{3}{4}\left(1-\nu^2\right)\frac{k}{R^{1/2}}\frac{d}{\delta^{3/2}}, \qquad (1)$$

where ν is the Poisson ratio of the sample, k is the spring constant of the cantilever, R is the radius of the polystyrene bead, d is the deflection of the cantilever, and δ is the sample indentation depth. The indentation depth can be calculated by subtracting the cantilever deflection d from the piezo displacement z [93, 94]. Evaluation of the indentation depth δ and elastic modulus E were performed in the retracting part of the force-displacement curves [95, 96]. Note that this Hertz model has the potential of overestimating by up to

25 % of the true elastic modulus, since the model neglects the adhesive effects and tends to underestimate the contact area [93-96].

5.2.4 Cell culture and imaging

Endothelial cells were isolated from porcine pulmonary arteries obtained from a local abattoir. The endothelial cells were cultivated in an incubator at 37 °C and 5% CO_2. The cell culture media consisted of M199 (GibcoBRL) and 10% fetal bovine serum (FBS) (Hyclone) supplemented with BME vitamins (Sigma), L-glutamine (GibcoBRL), penicillin and streptomycin (GibcoBRL), and BME amino acids (Sigma). The culture was maintained for approximately 1 week, at which point the cells reached confluence. They were then regularly passaged once a week. For this study, passages between four and ten were used for measurements. Trypsin-EDTA (1X, GibcoBRL) was used to detach cells for passaging and hydrogel inoculation. Endothelial cells suspended in M199 were inoculated directly onto a series of sterilized hydrogels and cultivated in an incubator for 20 hours. All optical images were taken using a phase contrast microscope.

5.3 Results and Discussion

The samples selected for this study were chosen for a number of important reasons. The copolymer hydrogels exhibit a range of elasticity and these particular materials have been successfully used as scaffolds for cellular systems. The copolymers chosen for this study also have well defined thermodynamic properties.

Figure 5.1 summarizes the swelling transitions in HEMA-MAETAC copolymer hydrogels. Increasing proportions of positively charged MAETAC monomers produce an

overall trend toward increasing swelling in equilibrium. The hydrogels prepared at

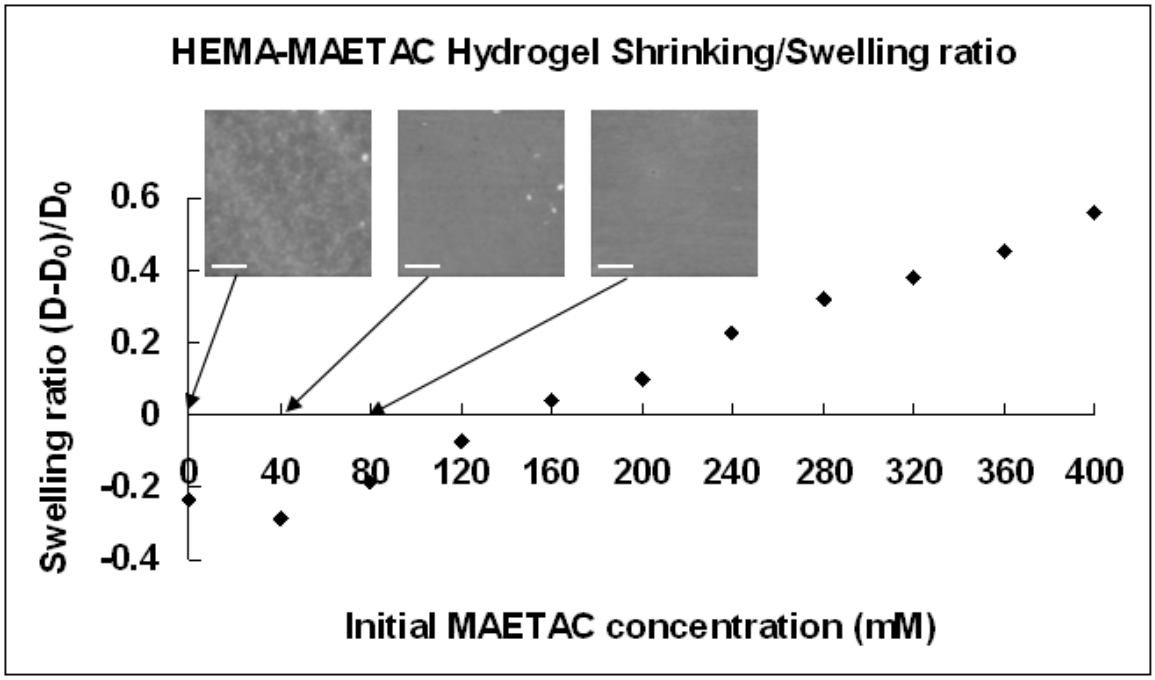

Figure 5.1: HEMA-MAETAC equilibrium swelling behavior as a function of copolymer hydrogel charge with a fixed of 154 mM NaCl bath salt concentration. Adding increasing proportions of positively charged monomers produces increasingly swollen states. Inset scale bars = 2 µm.

MAETAC concentrations less than or equal to 120 mM undergo collapsed transitions when they are equilibrated at physiologic ion strengths (154mM NaCl). These hydrogels that undergo collapse transitions initially show cloudy gels but subsequently become transparent in time. The swollen hydrogels, for MAETAC concentrations higher than 120 mM, are transparent without cloudiness but become increasingly fragile with increasing swelling.

The inset figures show the AFM surface nanotopography images for the neutral HEMA (0 mM), basic HEMA-MAETAC hydrogels prepared with +40 mM and +80 mM MAETAC concentrations, respectively. It was not possible to scan and image HEMA-MAETAC hydrogel samples with charges of +120 mM or greater due to their excessively low elastic moduli. The surface roughness of the HEMA-MAETAC hydrogels lessened progressively with increasing MAETAC concentrations.

Figure 5.2-a, 5.2-b, and 5.2-c show representative force-versus-displacement curves for a neutral HEMA hydrogel, a +200 mM HEMA-MAETAC copolymer hydrogel, and a +400 mM HEMA-MAETAC copolymer hydrogel in a 154 mM NaCl bath ion solution at 37 ^{o}C respectively. The inset sketches illustrate the 6-μm-diameter beaded probe before contact ($z < 0$), at the moment of contact with the gel surface ($z = 0$), and when the probe has indented to the gel ($z > 0$). The maximum indentation force is limited to 21 nN, which is equivalent to the maximum cantilever deflection and bead indentation for a given hydrogel sample.

Increasing proportions of charged monomers produced approaching-retracting curves with increasing hysteresis associated with the viscoelastic deformation and the adhesive properties of the hydrogel surface. The initial cantilever deflection towards the

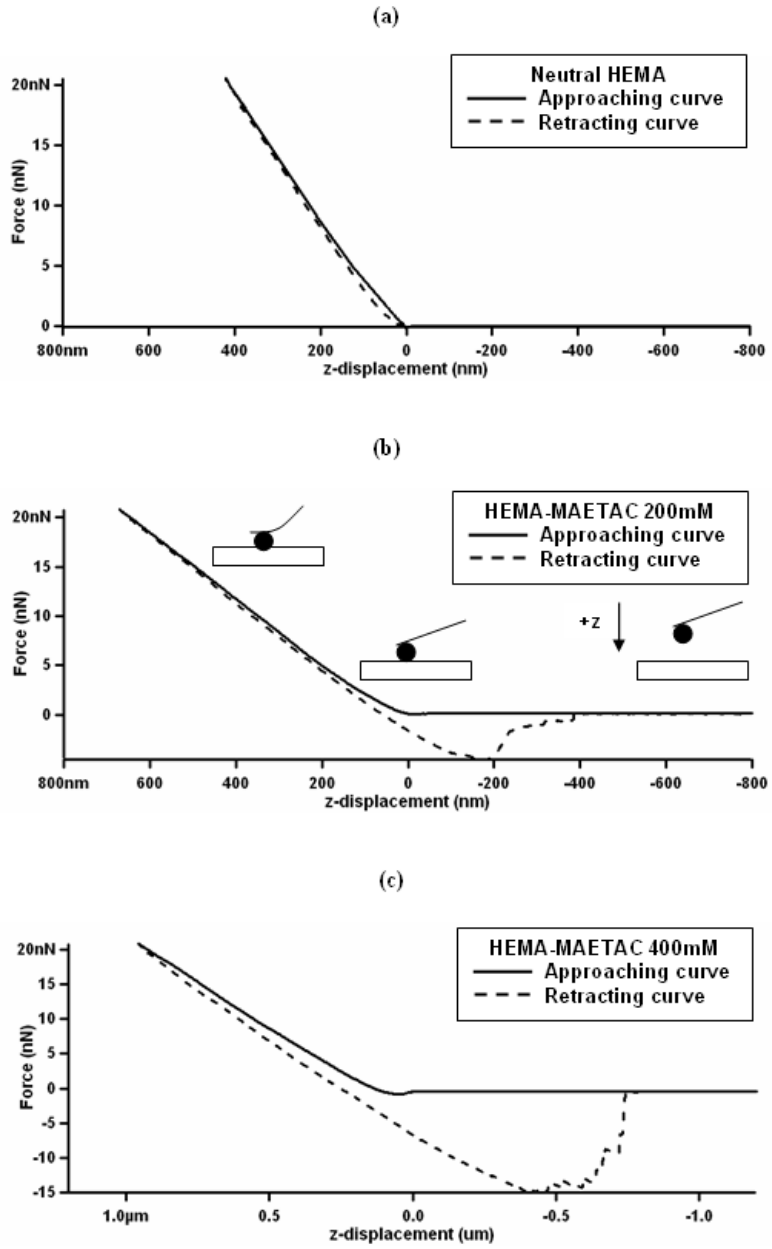

Figure 5.2: Force-displacement curves for a representative hydrogels in an approaching and retracting cycle. (a) Neutral HEMA (b) +200 mM HEMA-MAETAC (c) +400mM HEMA-MAETAC. The approach and retract curve hysteresis and the initial approach curve deflection occur in association with increasing charged monomer concentration.

hydrogel surface on approaching curves ("snap-in") and the final cantilever deflection on retracting curves ("snap-out") also increased with increasing proportions of positively charged MAETAC monomers. During snap-in and snap-out, a combination of van der Waals and electrostatic forces attracted the 6-μm polystyrene microsphere affixed to the cantilever. The increased charge density of HEMA-MAETAC hydrogel seemed to increase these attraction forces, resulting in a greater hysteresis.

When the maximum cantilever deflection was specified as a fixed value, the corresponding maximum indentation depth, δ, increased with increasing MAETAC concentrations as a result of the decreasing surface elasticity. In the case of a maximum cantilever deflection of 350 nm at 21 nN, Figure 5.3 shows eleven (11) different hydrogels with a range of monomer concentrations up to 400 mM in a 154-mM NaCl bath ion solution at 37 ^{o}C. Each symbol represents the averaged indentation depth, δ, from a total of fifty measurements at five different locations (ten at each location) with the error bar of corresponding standard deviation. Measurement uncertainty increased with more swollen hydrogels having corresponding lower surface elasticities.

Figure 5.4 shows the dependence of the Young's modulus estimation on the indentation depth based on retracting curves. Each symbol represents the averaged Young's modulus, E, from a total of fifty measurements at five different locations (ten at each location) with the error bar of corresponding standard deviation. For the more swollen hydrogels, Young's modulus estimates obtained from the retracting curves were more stable. In the analysis range, the Young's modulus, E, is nearly independent of the indentation depth. For the collapsed hydrogel (HEMA), which shows the highest surface elasticity, however, estimation of the Young's modulus was slightly increased with

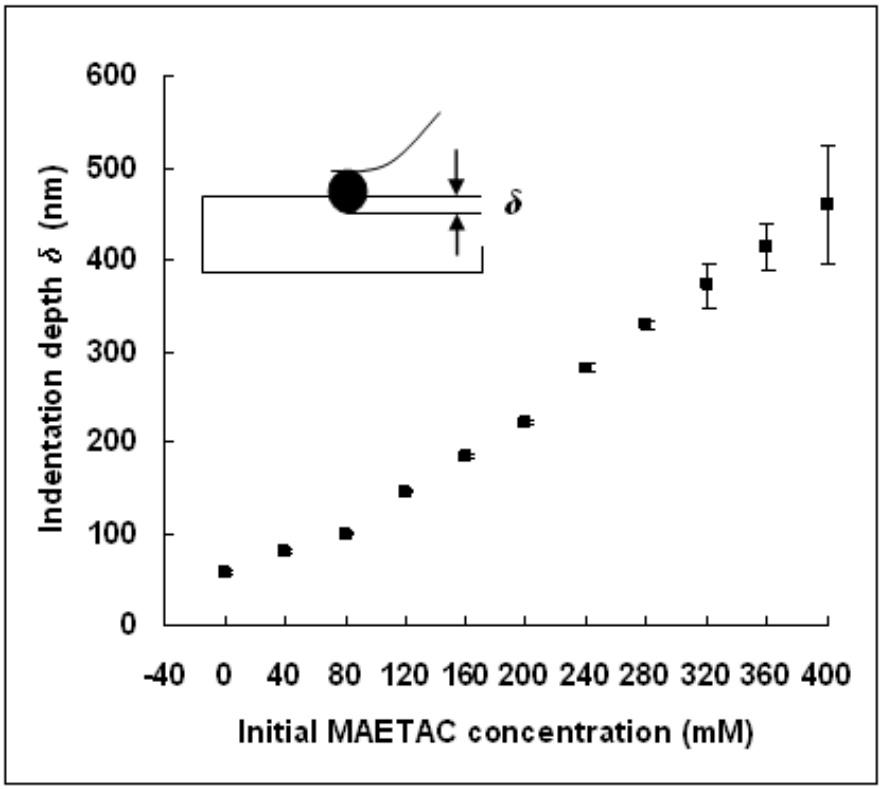

Figure 5.3: Indentation depth for a given cantilever deflection versus initially prepared hydrogel charged monomer concentration using a retracting curve analysis. The error bars represent the standard deviation of fifty measurements at five different locations (ten at each location) over the hydrogel surface.

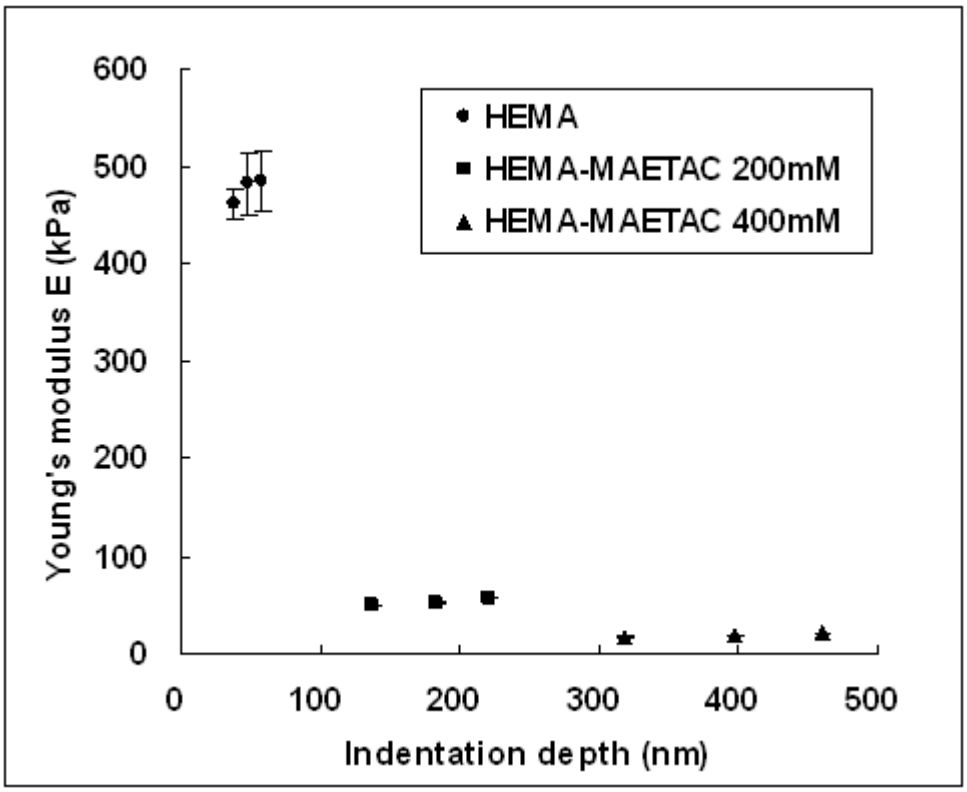

Figure 5.4: Young's modulus versus indentation depth using a retracting curve analysis.

increasing indentation depth, and this is attributed to the fact that uncertainties of contact *z*-point determination increased when the highly elastic surface allowed a relatively shallower indentation depth. Note that the use of the approaching curves in determining the Young's modulus tends to result in a bias because of the stepwise probe contact triggered by the van der Waals force interactions [95, 96].

Figure 5.5 summarizes the Young's modulus versus initially prepared charged monomer concentration based on the retracting force curve analysis. Each symbol represents the averaged Young's modulus, *E*, from a total of fifty measurements at five different locations (ten at each location) with the error bar of corresponding standard deviation. The four sets of data represent hydrogels that were equilibrated in physiologic saline solution (154 mM NaCl), M199 with 10% FBS (culture medium with serum, but no pH control), M199 without FBS containing 25 mM HEPES buffer (culture medium without serum, but with pH control), and M199 with 10% FBS containing 25 mM HEPES buffer (culture medium with serum and pH control). The temperature was kept at 37 ^{o}C in all cases.

Increasing the relative proportion of charged monomers produced a systematic decrease in the Young's modulus. Within the error tolerances, the Young's modulus for hydrogel equilibrated in physiologic saline is similar to those equilibrated in M199 media with FBS. In the absence of FBS and a controlled CO_2 environment, a white precipitate was observed in the solution and the errors associated with the corresponding Young's moduli were significantly larger. Including a HEPES buffer removed the precipitate and reduced the errors associated with the measurements.

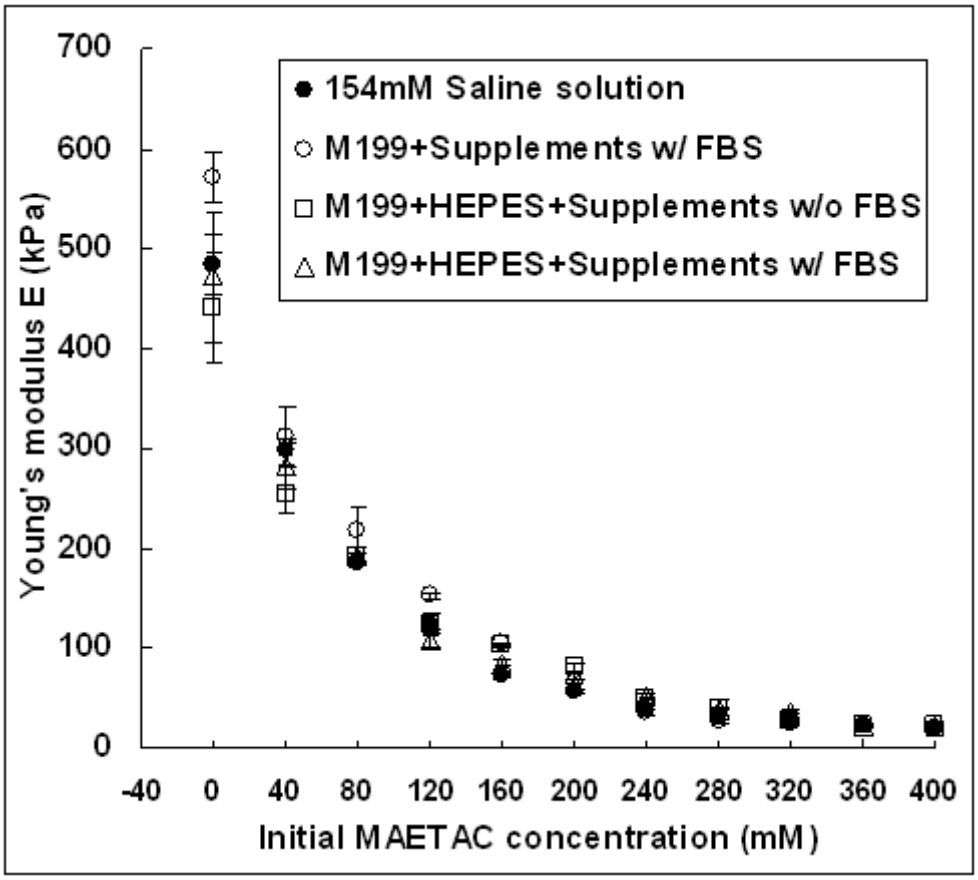

Figure 5.5: HEMA-MAETAC force spectroscopy estimates of the surface elasticity. Adding increasing proportions of positively charged monomers produces a decrease in the surface elasticity. The error bars represent the standard deviation of a total fifty measurements at five different locations (ten at each location) over the hydrogel surface. The four sets of data represent hydrogels that were equilibrated in 154 mM NaCl, M199 media with FBS, M199 media without FBS but containing 25 mM HEPES buffer, and M199 media with FBS containing 25 mM HEPES buffer.

Figure 5.6 shows a series of photomicrographs of porcine pulmonary artery endothelial cells (PPAECs) on the different hydrogels following 20 hours of growth. The hydrogels prepared with 0, +40 and +80 mM of MAETAC monomers promoted very little endothelial cell adhesion. In most cases the cells remained round and eventually died. Hydrogels prepared with MAETAC concentrations of +120 mM and higher promoted endothelial cell attachment with a “cobblestone” morphology. This agrees with the hypothesis that HEMA copolymer hydrogels with higher MAETAC concentrations and more positive surface charges allow enhanced cellular attachment.

Systematic changes in hydrogel monomer composition provide a valuable means for understanding the phase behavior of these materials. In general, increasing proportions of charged MAETAC monomers produce increasing swelling states at physiologic ion strengths. A corresponding decrease in elastic moduli is also produced. Most previous studies of this nature have only considered commercially available hydrogel materials as model systems. The strength of the present study is the correspondence between AFM measurements and well defined hydrogel thermodynamic states. This can be used as a guide for the synthesis of predefined matrices for a number of biotechnological applications.

Special considerations are noted on the elastic moduli estimation for different indentation depths, and the determination of the elastic moduli using either retracting or approaching force curve analysis. Estimates of the elastic moduli based on the retracting curve are less prone to systematic errors. For a given cantilever deflection, the indentation depth increases with increasing proportions of positively charged monomers. The decrease in surface elasticity is associated with greater swelling states.

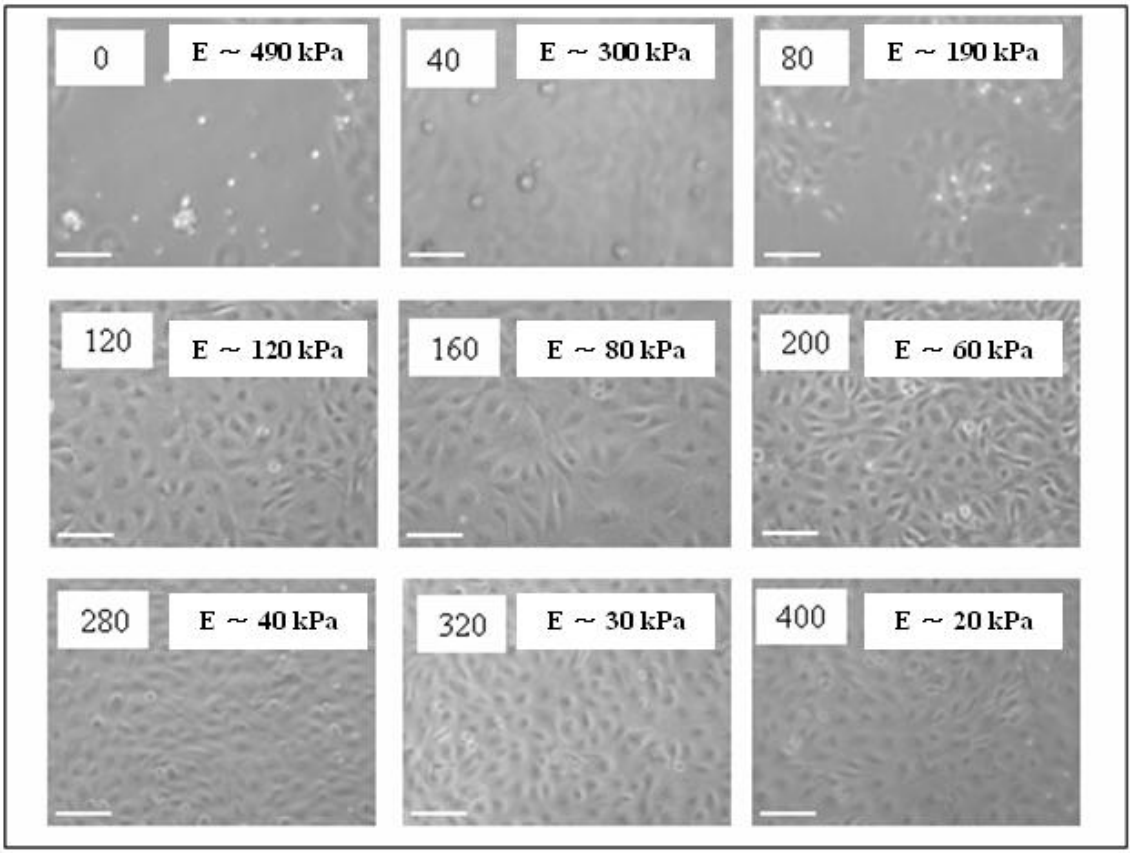

Figure 5.6: Endothelial cell morphologies as a function of prepared hydrogel charge after 20 hours of growth. Hydrogels prepared with 0, +40 or +80 mM MAETAC resist cellular attachment. Hydrogels prepared with charged monomer concentrations between +120 and +400 mM promote cellular attachment. Scale bars = 100 µm.

The lateral resolution in this study depends on the polystyrene bead used. If a schematic of the polystyrene (PS) sphere bead indentation is drawn, it will be clear that the indentation diameter φ, which determines lateral resolution, depends on indentation depth and radius of PS sphere. $\phi = 2\sqrt{2R\delta - \delta^2}$. Thus, the lateral resolution for this system is estimated to be in the order of a few microns.

The surface nanotopography of the HEMA-MAETAC hydrogels prepared with 0, +40 and +80 mM MAETAC were imaged successfully with AFM system. It was, however, not possible to image hydrogel samples with charges of +120 mM and greater. The relatively small elastic moduli of more swollen samples made it impossible to obtain stable surface image measurements. The surface nanotopography of the HEMA hydrogel was rougher than that of the +40 and +80 mM hydrogels.

During the polymerization process, the HEMA hydrogels with smaller proportions of charged MAETAC monomers became increasingly cloudy, indicating the presence of a phase separation. When these cloudy hydrogels were washed, they underwent a collapse transition to a denser transparent state. The surface roughness of the pure HEMA hydrogel may, therefore, be the result of the quenched disorder that occurs during the collapse transition following washing. Cloudiness was not observed in the HEMA-MAETAC hydrogels with concentrations higher than 120 mM. The hydrogels in this study were equilibrated in physiologic ion strengths for approximately one week in a Petri dish laid inside the laminar hood. Very slow kinetics have been observed in these materials [16]. In general, the swelling kinetics increase with the square of the hydrogel dimensions.

High charge density hydrogels are subject to ion condensation effects and the

restricted swelling produced by the finite polymer length. With increasing charge beyond a threshold limit Manning condensation will limit the charge density even if more charged monomers are added. In addition, the restricted polymer lengths will prevent further swelling of the network. This could provide an explanation for the elastic moduli observed at high charge densities. The highly swollen hydrogels are more likely to detach from the substrate, and thus the swollen hydrogels can substantially bias the AFM measurements to be unacceptable. The initial decrease in the swelling observed at +40 mM could be explained either by assuming that there are charged methacrylic acid monomers in the HEMA stock or by the steric interactions.

Normal atmospheric levels of carbon dioxide (CO_2) vary from 0.03% to 0.06%. As a result, when cell culture media is removed from a 5% CO_2 atmosphere provided by an incubator, there is a significant drop in the exposed CO_2 levels. When carbon dioxide dissolves in a medium, it tends to lower the solution's pH through the formation of carbonic acid. Lowering the ambient atmospheric CO_2, by removing a cell culture sample from a 5% CO_2 atmosphere, therefore, tends to drive the pH up. In the absence of a CO_2 atmosphere, the cell culture media used in this study formed precipitates. The presence of calcium or magnesium in the cell culture media can potentially give rise to a number of precipitates. In the absence of a 5% CO_2 environment the media pH can rise above 7.4. This in turn can give rise to small increases in hydroxide, OH^-, and phosphate ion, PO_4^{3-}, concentrations. The solubility product constant, K_{sp}, of calcium phosphate, $Ca_3(PO_4)_2$ is 2.07×10^{-33}, making calcium phosphate a likely candidate for a precipitate when the pH increases slightly. Magnesium phosphate, with a K_{sp} of 1.04×10^{-24}, is another strong candidate.

The ability to fabricate hydrogels with systematic changes in some physical quality, such as surface charge and elasticity, has a number of important applications in bioscience and engineering. In particular, the results of this study have important implications for the application of hydrogel materials for cellular scaffolds. A number of studies indicate that hydrogel surface charge and elasticity play an important role in promoting cellular attachment and proliferation [22-25].

As Figure 5.1 shows, increasing proportions of charged monomers can produce swelling transitions that reduce the equilibrium charge density compared to the prepared charge density. This is an important consideration when one is attempting to separate the effects of surface elasticity and charge density on cellular attachment. In addition to the mechanical effects of surface elasticity and non-specific binding forces produced by charge and van der Waals interactions, specific binding effects need to be considered. Serum proteins can be absorbed into the hydrogel surface in a charge- and composition-dependent manner. In general, increased surface charge densities produce increasing serum protein absorption. Neutral hydrogels, such as poly L-lactic acid, are often hydrolyzed in acid or base to produce charged carboxyl groups.

The results of this study have important implications for the recent interpretation that stiffer hydrogels promote cellular attachment and growth more readily than softer hydrogels. In this study, the softer, more flexible hydrogels clearly promote greater endothelial cell attachment. The more charged hydrogels, in this case, will also likely promote increased cellular adhesion through the absorption of adhesion ligands from the cell-culture media and through the charge-charge interactions between the cell and the hydrogel surface. The complex interaction between non-specific binding, specific binding,

and surface elasticity must be, therefore, carefully reconsidered.

5.4 Conclusion

Increasing concentrations of positively charged MAETAC monomers produced swelling transitions and decreasing surface elastic moduli when the total pregelation monomer concentration was maintained at 1.54 M. The HEMA-MAETAC copolymer hydrogels prepared with 0, +40 and +80 mM of MAETAC monomers promoted very little endothelial cell adhesion. However, the hydrogels with MAETAC concentrations of +120 mM and higher promoted endothelial cell attachment with cobblestone morphology.

CHAPTER 6

Conclusion

In order to develop microscale thermofluidic and biophysical sensors, characterization of dynamic responses of AFM cantilevers in liquid medium was systematically performed and practical applications of microcantilever sensors for thermofluidic and biophysical problems were provided.

Experimental verification of the Sader's viscous model far-away from a surface has been attempted for thermally induced shifts of the peak resonance response frequencies and the *Q*-factors of three different microcantilevers immersed in de-ionized water at controlled temperatures ranging from 10 to 70 °C. The peak resonance response frequency shifts are dominated by the temperature effects associated with the viscosity and density of de-ionized water, and the effect associated with the cantilever elasticity variation with temperature is far less substantial. Experimental investigation of the extended Sader's viscous model near a solid surface has been attempted for thermally induced shifts of the peak resonance response frequencies of three different microcantilevers immersed in de-ionized water near a solid surface at controlled temperatures ranging from 30 to 70 °C. The peak resonance response frequency shifts are dominated by the temperature effects associated with the viscous dissipative and inertial effect of de-ionized water, and the effect associated with the cantilever elasticity variation with temperature is far less substantial. Discrepancies of the predictions based on the extended Sader's viscous model near a solid surface, which assumes a parallel cantilever, are identified from the present measurements using inclined microcantilevers. The near-

wall temperature sensitivities of the resonance frequency shifts increase with increasing h/L^2 (a thicker and shorter cantilever), increasing E/ρ_c (a stiffer cantilever), and decreasing cantilever width b.

Theoretical modification of the extended Sader's viscous model has been attempted to accommodate the adsorbed mass and the spring constant change of a microcantilever resulting from the effect of adsorption-induced surface stress change. The peak resonance response frequency shifts of microcantilevers are dominated by the hydrodynamic loadings associated with the viscosity and density change of saline solution. The spring constant change due to adsorption-induced surface stress change also influences the resonance frequency shifts and the effect associated with the adsorbed mass of ions is negligible. The spring constant changes of four different microcantilevers in saline solution were determined with the modified Sader's model and measured experimental data, and the stiffness of tested microcantilevers in saline solution tends to increase with increasing salt concentration and the absolute value of concentration detection sensitivity of tested microcantilevers decreases due to the stiffening of cantilevers.

With these fundamental understanding of dynamic responses of AFM cantilevers in liquid medium, a new concept of a near-wall thermometry sensor (a novel SThM) using a tipless microcantilever in aqueous medium has been experimentally validated by conducting careful thermal field measurements. The experimental calibration, accounting for the near-wall hydrodynamic interference effect, has been utilized to correlate the resonance frequency of a microcantilever with the temperature of aqueous medium. The microscale temperature measurements using this sensor agree well with the calculated

predictions. To improve spatial resolution and thermal sensitivity of this sensor, use of a shorter, thicker, and narrower microcantilever made of silicon dioxide is recommended for further study based on theoretical predictions and experimental results. This microcantilever sensor can also lessen the complexity and mitigate the high cost associated with existing microfabricated thermocouples or thermoresistive sensors. It is expected that successful implementation of self-excitation detection schemes to provide quasi-real time and highly accurate detection of the microcantilever resonance frequency will be essential to further develop microcantilever thermometry sensor for real-time response to highly transient thermal fields.

Finally, surface nanomechanical property of polyelectrolyte hydrogels (HEMA-MAETAC) has been probed using a micro bead-affixed microcantilever in liquid medium to investigate the biophysical implication of this property on cell-substrate interactions. Increasing concentrations of positively charged MAETAC monomers produced swelling transitions of hydrogels and decreasing surface elastic moduli when the total pregelation monomer concentration was maintained at 1.54 M. A comprehensive theoretical investigation is recommended to explain the major factor inducing surface elasticity change of polyelectrolyte hydrogels. The HEMA-MAETAC copolymer hydrogels prepared with 0, +40 and +80 mM of MAETAC monomers promoted very little endothelial cell adhesion and resist cell proliferation. However, the hydrogels with MAETAC concentrations of +120 mM and higher promoted endothelial cell attachment with cobblestone morphology.

REFERENCES

1. Binnig, G., C.F. Quate, and C. Gerber, *Atomic Force Microscope.* Physical Review Letters, 1986. **56**(9): p. 930-933.
2. Giessibl, F.J., *Advances in atomic force microscopy.* Reviews of Modern Physics, 2003. **75**(3): p. 949-983.
3. Heinz, W.F. and J.H. Hoh, *Spatially resolved force spectroscopy of biological surfaces using the atomic force microscope.* Trends in Biotechnology, 1999. **17**(4): p. 143-150.
4. *Opensource Handbook of Nanoscience and Nanotechnology*: Wikibooks.
5. Martin, Y., C.C. Williams, and H.K. Wickramasinghe, *Atomic Force Microscope Force Mapping and Profiling on a Sub 100-a Scale.* Journal of Applied Physics, 1987. **61**(10): p. 4723-4729.
6. Riethmuller, W. and W. Benecke, *Thermally Excited Silicon Microactuators.* Ieee Transactions on Electron Devices, 1988. **35**(6): p. 758-763.
7. Stemme, G., *Resonant silicon sensors.* Journal of Micromechanics and Microengineering, 1991. **1**(2): p. 113-125.
8. Allison, D.P., et al., *Immobilization of DNA for Scanning Probe Microscopy.* Proceedings of the National Academy of Sciences of the United States of America, 1992. **89**(21): p. 10129-10133.
9. Thundat, T., et al., *Atomic Force Microscopy of DNA on Mica and Chemically Modified Mica.* Scanning Microscopy, 1992. **6**(4): p. 911-918.

10. Su, M., S.U. Li, and V.P. Dravid, *Microcantilever resonance-based DNA detection with nanoparticle probes.* Applied Physics Letters, 2003. **82**(20): p. 3562-3564.

11. Lee, J.H., T.S. Kim, and K.H. Yoon, *Effect of mass and stress on resonant frequency shift of functionalized Pb(Zr0.52Ti0.48)O-3 thin film microcantilever for the detection of C-reactive protein.* Applied Physics Letters, 2004. **84**(16): p. 3187-3189.

12. Gupta, A., D. Akin, and R. Bashir, *Single virus particle mass detection using microresonators with nanoscale thickness.* Applied Physics Letters, 2004. **84**(11): p. 1976-1978.

13. Lavrik, N.V., M.J. Sepaniak, and P.G. Datskos, *Cantilever transducers as a platform for chemical and biological sensors.* Review of Scientific Instruments, 2004. **75**(7): p. 2229-2253.

14. Raiteri, R., et al., *Micromechanical cantilever-based biosensors.* Sensors and Actuators B-Chemical, 2001. **79**(2-3): p. 115-126.

15. Burnham, N.A. and R.J. Colton, *Measuring the Nanomechanical Properties and Surface Forces of Materials Using an Atomic Force Microscope.* Journal of Vacuum Science & Technology a-Vacuum Surfaces and Films, 1989. **7**(4): p. 2906-2913.

16. English, A.E., E.R. Edelman, and T. Tanaka, *Polymer Hydrogel Phase Transitions*, in *Experimental Methods in Polymer Science*. 2000, Academic Press: Cambridge. p. 547-589.

17. English, A.E., et al., *Equilibrium swelling properties of polyampholytic hydrogels.* Journal of Chemical Physics, 1996. **104**(21): p. 8713-8720.

18. English, A.E., T. Tanaka, and E.R. Edelman, *Polyelectrolyte hydrogel instabilities in ionic solutions.* Journal of Chemical Physics, 1996. **105**(23): p. 10606-10613.

19. English, A.E., T. Tanaka, and E.R. Edelman, *Equilibrium and non-equilibrium phase transitions in copolymer polyelectrolyte hydrogels.* Journal of Chemical Physics, 1997. **107**(5): p. 1645-1654.

20. English, A.E., T. Tanaka, and E.R. Edelman, *Polymer and solution ion shielding in polyampholytic hydrogels.* Polymer, 1998. **39**(24): p. 5893-5897.

21. English, A.E., T. Tanaka, and E.R. Edelman, *Polyampholytic hydrogel swelling transitions: Limitations of the Debye-Huckel law.* Macromolecules, 1998. **31**(6): p. 1989-1995.

22. Vanwachem, P.B., et al., *Adhesion of Cultured Human-Endothelial Cells onto Methacrylate Polymers with Varying Surface Wettability and Charge.* Biomaterials, 1987. **8**(5): p. 323-328.

23. Boura, C., et al., *Endothelial cells grown on thin polyelectrolyte mutlilayered films: an evaluation of a new versatile surface modification.* Biomaterials, 2003. **24**(20): p. 3521-3530.

24. Schneider, G.B., et al., *The effect of hydrogel charge density on cell attachment.* Biomaterials, 2004. **25**(15): p. 3023-3028.

25. Boura, C., et al., *Endothelial cell - interactions with polyelectrolyte multilayer films.* Biomaterials, 2005. **26**(22): p. 4568-4575.

26. Chen, G.Y., et al., *Resonance Response of Scanning Force Microscopy Cantilevers.* Review of Scientific Instruments, 1994. **65**(8): p. 2532-2537.

27. Baselt, D.R., G.U. Lee, and R.J. Colton, *Biosensor based on force microscope*

technology. Journal of Vacuum Science & Technology B, 1996. **14**(2): p. 789-793.

28. Datskos, P.G., et al., *Remote infrared radiation detection using piezoresistive microcantilevers*. Applied Physics Letters, 1996. **69**(20): p. 2986-2988.

29. Oden, P.I., et al., *Viscous drag measurements utilizing microfabricated cantilevers.* Applied Physics Letters, 1996. **68**(26): p. 3814-3816.

30. Thundat, T., P.I. Oden, and R.J. Warmack, *Microcantilever sensors.* Microscale Thermophysical Engineering, 1997. **1**(3): p. 185-199.

31. Lavrik, N.V. and P.G. Datskos, *Femtogram mass detection using photothermally actuated nanomechanical resonators.* Applied Physics Letters, 2003. **82**(16): p. 2697-2699.

32. Hwang, K.S., et al., *In-situ quantitative analysis of a prostate-specific antigen (PSA) using a nanomechanical PZT cantilever.* Lab on a Chip, 2004. **4**(6): p. 547-552.

33. Gupta, A.K., et al., *Anomalous resonance in a nanomechanical biosensor.* Proceedings of the National Academy of Sciences of the United States of America, 2006. **103**(36): p. 13362-13367.

34. Roters, A. and D. Johannsmann, *Distance-dependent noise measurements in scanning force microscopy.* Journal of Physics-Condensed Matter, 1996. **8**(41): p. 7561-7577.

35. Tamayo, J., et al., *Chemical sensors and biosensors in liquid environment based on microcantilevers with amplified quality factor.* Ultramicroscopy, 2001. **86**(1-2): p. 167-173.

36. Mehta, A., et al., *Manipulation and controlled amplification of Brownian motion*

of microcantilever sensors. Applied Physics Letters, 2001. **78**(11): p. 1637-1639.

37. Tamayo, J. and L.M. Lechuga, *Decrease of the resonance bandwidth of micromechanical oscillators by phase control of the driving force.* Applied Physics Letters, 2003. **82**(17): p. 2919-2921.

38. Lavrik, N.V., et al., *Enhanced chemi-mechanical transduction at nanostructured interfaces.* Chemical Physics Letters, 2001. **336**(5-6): p. 371-376.

39. Sader, J.E., *Frequency response of cantilever beams immersed in viscous fluids with applications to the atomic force microscope.* Journal of Applied Physics, 1998. **84**(1): p. 64-76.

40. Green, C.P. and J.E. Sader, *Torsional frequency response of cantilever beams immersed in viscous fluids with applications to the atomic force microscope.* Journal of Applied Physics, 2002. **92**(10): p. 6262-6274.

41. Chon, J.W.M., P. Mulvaney, and J.E. Sader, *Experimental validation of theoretical models for the frequency response of atomic force microscope cantilever beams immersed in fluids.* Journal of Applied Physics, 2000. **87**(8): p. 3978-3988.

42. Boskovic, S., et al., *Rheological measurements using microcantilevers.* Journal of Rheology, 2002. **46**(4): p. 891-899.

43. Green, C.P. and J.E. Sader, *Frequency response of cantilever beams immersed in viscous fluids near a solid surface with applications to the atomic force microscope.* Journal of Applied Physics, 2005. **98**(11).

44. White, F.M., *Fluid Mechanics*. 5th ed. 2003, New York: McGraw-Hill.

45. McSkimin, H.J., *Measurement of Elastic Constants at Low Temperatures by Means of Ultrasonic Waves - Data for Silicon and Germanium Single Crystals,*

and for Fused Silica. Journal of Applied Physics, 1953. **24**(8): p. 988-997.

46. Han, J.Q., et al., *Dependence of the resonance frequency of thermally excited microcantilever resonators on temperature.* Sensors and Actuators a-Physical, 2002. **101**(1-2): p. 37-41.

47. Shen, F., et al., *Thermal effects on coated resonant microcantilevers.* Sensors and Actuators a-Physical, 2001. **95**(1): p. 17-23.

48. Mertens, J., et al., *Effects of temperature and pressure on microcantilever resonance response.* Ultramicroscopy, 2003. **97**(1-4): p. 119-126.

49. Sader, J.E., J.W.M. Chon, and P. Mulvaney, *Calibration of rectangular atomic force microscope cantilevers.* Review of Scientific Instruments, 1999. **70**(10): p. 3967-3969.

50. Naik, T., E.K. Longmire, and S.C. Mantell, *Dynamic response of a cantilever in liquid near a solid wall.* Sensors and Actuators a-Physical, 2003. **102**(3): p. 240-254.

51. Clarke, R.J., et al., *Stochastic elastohydrodynamics of a microcantilever oscillating near a wall.* Physical Review Letters, 2006. **96**(5).

52. Paul, M.R., M.T. Clark, and M.C. Cross, *The stochastic dynamics of micron and nanoscale elastic cantilevers in fluid: fluctuations from dissipation.* Nanotechnology, 2006. **17**(17): p. 4502-4513.

53. Chen, G.Y., et al., *Adsorption-Induced Surface Stress and Its Effects on Resonance Frequency of Microcantilevers.* Journal of Applied Physics, 1995. **77**(8): p. 3618-3622.

54. Thundat, T., et al., *Detection of Mercury-Vapor Using Resonating*

Microcantilevers. Applied Physics Letters, 1995. **66**(13): p. 1695-1697.

55. Fritz, J., et al., *Translating biomolecular recognition into nanomechanics.* Science, 2000. **288**(5464): p. 316-318.

56. Hu, Z.Y., T. Thundat, and R.J. Warmack, *Investigation of adsorption and absorption-induced stresses using microcantilever sensors.* Journal of Applied Physics, 2001. **90**(1): p. 427-431.

57. Dareing, D.W. and T. Thundat, *Simulation of adsorption-induced stress of a microcantilever sensor.* Journal of Applied Physics, 2005. **97**(4).

58. Huang, G.Y., W. Gao, and S.W. Yu, *Model for the adsorption-induced change in resonance frequency of a cantilever.* Applied Physics Letters, 2006. **89**(4).

59. Lu, P., et al., *Surface stress effects on the resonance properties of cantilever sensors.* Physical Review B, 2005. **72**(8).

60. Cherian, S. and T. Thundat, *Determination of adsorption-induced variation in the spring constant of a microcantilever.* Applied Physics Letters, 2002. **80**(12): p. 2219-2221.

61. Cherian, S., A. Mehta, and T. Thundat, *Investigating the mechanical effects of adsorption of Ca2+ ions on a silicon nitride microcantilever surface.* Langmuir, 2002. **18**(18): p. 6935-6939.

62. Kim, S. and K.D. Kihm, *Experimental verification of the temperature effects on Sader's model for multilayered cantilevers immersed in an aqueous medium.* Applied Physics Letters, 2006. **89**(6).

63. Kim, S. and K.D. Kihm, *Temperature dependence of the near-wall oscillation of microcantilevers submerged in liquid environment.* Applied Physics Letters, 2007.

90(8).

64. Lachut, M.J. and J.E. Sader, *Effect of surface stress on the stiffness of cantilever plates.* Physical Review Letters, 2007. **99**(20).

65. Wang, G.F. and X.Q. Feng, *Effects of surface elasticity and residual surface tension on the natural frequency of microbeams.* Applied Physics Letters, 2007. **90**(23).

66. Shi, L. and A. Majumdar, *Recent developments in micro and nanoscale thermometry.* Microscale Thermophysical Engineering, 2001. **5**(4): p. 251-265.

67. Cahill, D.G., K. Goodson, and A. Majumdar, *Thermometry and thermal transport in micro/nanoscale solid-state devices and structures.* Journal of Heat Transfer-Transactions of the Asme, 2002. **124**(2): p. 223-241.

68. Shi, L. and A. Majumdar, *Thermal transport mechanisms at nanoscale point contacts.* Journal of Heat Transfer-Transactions of the Asme, 2002. **124**(2): p. 329-337.

69. Roh, H.H., et al., *Novel nanoscale thermal property imaging technique: The 2 omega method. I. Principle and the 2 omega signal measurement.* Journal of Vacuum Science & Technology B, 2006. **24**(5): p. 2398-2404.

70. Roh, H.H., et al., *Novel nanoscale thermal property imaging technique: The 2 omega method. II. Demonstration and comparison.* Journal of Vacuum Science & Technology B, 2006. **24**(5): p. 2405-2411.

71. Li, M.H. and Y.B. Gianchandani, *Applications of a low contact force polyimide shank bolometer probe for chemical and biological diagnostics.* Sensors and Actuators a-Physical, 2003. **104**(3): p. 236-245.

72. Watanabe, M.S., et al. *Micro-thermocouple probe for measurement of cellular thermal responses*. in *27th Annual Conference 2005 IEEE EMB*. 2005.

73. Kim, H.J., K.D. Kihm, and J.S. Allen, *Examination of ratiometric laser induced fluorescence thermometry for microscale spatial measurement resolution.* International Journal of Heat and Mass Transfer, 2003. **46**(21): p. 3967-3974.

74. Park, J.S., C.K. Choi, and K.D. Kihm, *Temperature measurement for a nanoparticle suspension by detecting the Brownian motion using optical serial sectioning microscopy (OSSM).* Measurement Science & Technology, 2005. **16**(7): p. 1418-1429.

75. Kim, I.T. and K.D. Kihm, *Full-field and real-time surface plasmon resonance imaging ththermometry.* Optics Letters, 2007. **32**(23): p. 3456-3458.

76. Paik, S.W., et al., *Spatially and temporally resolved temperature measurements for slow evaporating sessile drops heated by a microfabricated heater array.* Journal of Heat Transfer-Transactions of the Asme, 2007. **129**(8): p. 966-976.

77. Bruun, H.H., *Hot-wire Anemometry*. 1995, Oxford Press: London. p. 19-70.

78. Goldstein, R.J., *Fluid Mechanics Measurements*. 1983, Hemisphere Publishing Co.: Washington D.C. p. 99-144.

79. Lee, S.P. and S.K. Kauh, *A new approach to enhance the sensitivity of a hot-wire anemometer and static response analysis of a variable-temperature anemometer.* Experiments in Fluids, 1997. **22**(3): p. 212-219.

80. Tamayo, J., *Study of the noise of micromechanical oscillators under quality factor enhancement via driving force control.* Journal of Applied Physics, 2005. **97**(4).

81. Discher, D.E., P. Janmey, and Y.L. Wang, *Tissue cells feel and respond to the*

stiffness of their substrate. Science, 2005. **310**(5751): p. 1139-1143.

82. Pelham, R.J. and Y.L. Wang, *Cell locomotion and focal adhesions are regulated by substrate flexibility.* Proceedings of the National Academy of Sciences of the United States of America, 1997. **94**(25): p. 13661-13665.

83. Engler, A., et al., *Substrate compliance versus ligand density in cell on gel responses.* Biophysical Journal, 2004. **86**(1): p. 617-628.

84. Wong, J.Y., et al., *Directed movement of vascular smooth muscle cells on gradient-compliant hydrogels.* Langmuir, 2003. **19**(5): p. 1908-1913.

85. Deroanne, C.F., C.M. Lapiere, and B.V. Nusgens, *In vitro tubulogenesis of endothelial cells by relaxation of the coupling extracellular matrix-cytoskeleton.* Cardiovascular Research, 2001. **49**(3): p. 647-658.

86. Engler, A.J., et al., *Matrix elasticity directs stem cell lineage specification.* Cell, 2006. **126**(4): p. 677-689.

87. Dimitriadis, E.K., et al., *Determination of elastic moduli of thin layers of soft material using the atomic force microscope.* Biophysical Journal, 2002. **82**(5): p. 2798-2810.

88. Domke, J. and M. Radmacher, *Measuring the elastic properties of thin polymer films with the atomic force microscope.* Langmuir, 1998. **14**(12): p. 3320-3325.

89. Kim, S.H., et al., *AFM and SFG studies of pHEMA-based hydrogel contact lens surfaces in saline solution: adhesion, friction, and the presence of non-crosslinked polymer chains at the surface.* Biomaterials, 2002. **23**(7): p. 1657-1666.

90. Mahaffy, R.E., et al., *Scanning probe-based frequency-dependent microrheology of polymer gels and biological cells.* Physical Review Letters, 2000. **85**(4): p.

880-883.

91. Radmacher, M., M. Fritz, and P.K. Hansma, *Imaging Soft Samples with the Atomic-Force Microscope - Gelatin in Water and Propanol.* Biophysical Journal, 1995. **69**(1): p. 264-270.

92. Suzuki, A., M. Yamazaki, and Y. Kobiki, *Direct observation of polymer gel surfaces by atomic force microscopy.* Journal of Chemical Physics, 1996. **104**(4): p. 1751-1757.

93. Chizhik, S.A., et al., *Micromechanical properties of elastic polymeric materials as probed by scanning force microscopy.* Langmuir, 1998. **14**(10): p. 2606-2609.

94. Tsukruk, V.V., et al., *Probing of micromechanical properties of compliant polymeric materials.* Journal of Materials Science, 1998. **33**(20): p. 4905-4909.

95. Koffas, T.S., et al., *Effect of equilibrium bulk water content on the humidity-dependent surface mechanical properties of hydrophilic contact lenses studied by atomic force microscopy.* Langmuir, 2003. **19**(8): p. 3453-3460.

96. Opdahl, A., et al., *Surface mechanical properties of pHEMA contact lenses: Viscoelastic and adhesive property changes on exposure to controlled humidity.* Journal of Biomedical Materials Research Part A, 2003. **67A**(1): p. 350-356.

97. Landau, L.D. and E.M. Lifshitz, *Theory of Elasticity*. 1970, Oxford: Pergamon.

98. Sandberg, R., et al., *Temperature and pressure dependence of resonance in multi-layer microcantilevers.* Journal of Micromechanics and Microengineering, 2005. **15**(8): p. 1454-1458.

99. Rosenhead, L., *Laminar Boundary Layers*. 1963, Oxford: Clarendon.

100. Abramowitz, M. and I.A. Stegun, *Handbook of Mathematical Functions*. 1972,

New York: Dover.

APPENDIX

APPENDIX

Mathematical derivations for the extended Sader's model

In this appendix, the formal derivation of the extended Sader's model is presented by modifying the original Sader's viscous model [39]. The original Sader's viscous model which theoretically predicts the frequency response of cantilever beams immersed in viscous fluid has several fundamental restrictions. These are the amplitude of vibration must be small, the fluid must be incompressible, and the length of the beam must greatly exceed its nominal width. Most AFM cantilever beams in viscous fluid satisfy these restriction and the thermal frequency spectra of AFM cantilever beams in viscous fluid can be successfully calculated by the original Sader's viscous model.

The general assumptions and approximations implemented in the Sader's viscous models are (1) the cross section of the beam is uniform over its entire length; (2) The length of the beam L greatly exceeds its nominal width b; (3) The beam is an isotropic linearly elastic solid and internal frictional effects are negligible; (4) The amplitude of vibration of the beam is far smaller than any length scale in the beam geometry. Since the amplitude of vibration is small, all nonlinear convective inertial effects in the fluid can be neglected, and the hydrodynamic loading on the beam will be a linear function of its displacement. Also, the velocity field in the fluid will vary very slowly along the length of the beam in comparison to chordwise variations across its width because of second assumption. Therefore, the velocity field at any point along the beam is well approximated by that of an infinitely long rigid beam executing transverse oscillations

with the same amplitude. This approximation will be exploited to formulate the hydrodynamic function Γ(ω) of cantilever beams that are circular and rectangular in cross section and since the dominant length scale in the flow is the nominal width b, then the appropriate Reynolds number Re for flow is given by

$$\mathrm{Re}(T) = \frac{\rho(T)\omega b^2}{4\eta(T)}, \tag{A1}$$

where T is temperature, $\rho(T)$ and $\eta(T)$ are the density and viscosity of the fluid, respectively, whereas ω is a characteristic radial frequency of the vibration, that is $2\pi f$.

The governing equation for the dynamic deflection function $w(x,t)$ of the beam [97] is given by

$$E(T)I\frac{\partial^4 w(x,t)}{\partial x^4} + \mu\frac{\partial^2 w(x,t)}{\partial t^2} = F(x,t) \tag{A2}$$

where E is Young's modulus, T is temperature, I is the moment of inertia of the cantilever, μ is the mass per unit length of the cantilever, F is the external applied force per unit length, x is the spatial coordinate along the length of the cantilever, and t is time. And the Young's modulus of cantilever beam can be approximated [98] by

$$E(T) = E(T_0) + \frac{dE}{dT}(T - T_0) \tag{A3}$$

where T is temperature, T_0 is the reference temperature, and dE/dT is the thermal dependence of Young's modulus. The boundary conditions for Eq. (A2) are the usual

clamped and free end conditions

$$\left[w(x,t) = \frac{\partial w(x,t)}{\partial x} \right]_{x=0} = \left[\frac{\partial^2 w(x,t)}{\partial x^2} = \frac{\partial^3 w(x,t)}{\partial x^3} \right]_{x=L} = 0 \tag{A4}$$

where L is the length of the beam. Now scale the spatial variable x with the length of the beam L and take the Fourier transform of Eq. (A2) to obtain

$$\frac{E(T)I}{L^4} \frac{d^4 \hat{W}(x|\omega)}{dx^4} - \mu\omega^2 \hat{W}(x|\omega) = \hat{F}(x|\omega), \tag{A5}$$

where

$$\hat{X}(x|\omega) = \int_{-\infty}^{\infty} X(x|\omega) e^{i\omega t} dt \tag{A6}$$

for any function of time X and for simplicity of notation, the spatial variable x in Eq. (A5) refers to its scaled quantity.

For a cantilever beam moving in a fluid, the external applied load can be separated into two contributions:

$$\hat{F}(x|\omega) = \hat{F}_{hydro}(x|\omega) + \hat{F}_{drive}(x|\omega). \tag{A7}$$

where the first component in Eq. (A7) is a hydrodynamic loading component due to the motion of the fluid around the beam, whereas the second term is a driving force that excites the beam. To proceed with the analysis, the general form of first term is required. Therefore, the Fourier transformed equations of motion for the fluid is examined.

$$\nabla \hat{u} = 0, \qquad -\nabla \hat{P} + \eta \nabla^2 \hat{u} = -i\rho\omega \hat{u}, \tag{A8}$$

where $\hat{u}$ is the velocity field, $\hat{P}$ is the pressure. From Eq. (A8) the general from of hydrodynamic loading component is given by

$$\hat{F}_{hydro}(x|\omega) = \frac{\pi}{4}\rho\omega^2 b^2 \Gamma(\omega) \hat{W}(x|\omega), \tag{A9}$$

where the ‘‘hydrodynamic function’’ Γ(ω) is dimensionless and is obtained from the solution of Eq. (A8) for a rigid beam, with identical cross section to that of the cantilever beam, undergoing transverse oscillatory motion. For a beam that is circular in cross section, the exact analytical result for $\Gamma_{circular}(\omega)$ is well known [99], and is given by

$$\Gamma_{circular}(\omega) = 1 + \frac{4iK_1(-i\sqrt{i\,\mathrm{Re}})}{\sqrt{i\,\mathrm{Re}}K_0(-i\sqrt{i\,\mathrm{Re}})}, \tag{A10}$$

where $\mathrm{Re}=\rho\omega b^2/(4\eta)$, as defined in Eq. (A1), whereas b is the diameter of the cylinder, and the functions K_0 and K_1 are modified Bessel functions of the third kind [100]. For a beam that is rectangular in cross section, the hydrodynamic function is formulated with an approximate empirical correction function for Eq. (A10) as

$$\Gamma_{rectangular}(\omega) = \Omega(\omega)\Gamma_{circular}(\omega), \tag{A11}$$

where $\Omega(\omega)$ is the correction function. The real and imaginary parts of $\Omega(\omega)$ is expressed as

$$\begin{aligned}\Omega_r(\tau) = (&0.91324 - 0.48274\tau + 0.46842\tau^2 - 0.12886\tau^3 \\ &+ 0.044055\tau^4 - 0.0035117\tau^5 + 0.00069085\tau^6) \\ &/(1 - 0.56964\tau + 0.4869\tau^2 - 0.13444\tau^3 \\ &+ 0.045155\tau^4 - 0.0035862\tau^5 + 0.00069085\tau^6),\end{aligned} \tag{A12a}$$

$$\begin{aligned}\Omega_i(\tau) = (&-0.024134 - 0.029256\tau + 0.016294\tau^2 \\ &- 0.00010961\tau^3 + 0.000064577\tau^4 \\ &- 0.00004451\tau^5)/(1 - 0.59702\tau + 0.55182\tau^2 \\ &- 0.18357\tau^3 + 0.079156\tau^4 - 0.014369\tau^5 + 0.0028361\tau^6),\end{aligned} \tag{A12b}$$

where $\tau = \log_{10}(\mathrm{Re})$ and $\Omega(\omega) = \Omega_r(\omega) + i\,\Omega_i(\omega)$. This approximate hydrodynamic function $\Gamma_{rectangular}(\omega)$ is accurate to within 0.1% over the entire range $\mathrm{Re} \in [10^{-6}, 10^4]$.

For the case that the cantilever beam is excited by thermal Brownian motion of the molecules in the fluid, it is clear that external driving force being applied to the beam is uncorrelated in position and is stochastic in nature. Thus, $\hat{F}_{drive}(x|\omega) = \hat{F}_{drive}(\omega)$. The expectation value of the potential energy for each mode of the beam must be identically equal to the thermal energy $1/2k_BT$, where k_B is Boltzmann's constant and T is absolute temperature. To evaluate the magnitudes of each of these driving forces, the modes of the damped cantilever beam must be decomposed into the modes of the undamped beam, since any damping will couple all modes. The undamped modes of a cantilever beam are given by

$$\phi_n(x) = (\cos C_n x - \cosh C_n x) + \frac{\cos C_n + \cosh C_n}{\sin C_n + \sinh C_n}(\sinh C_n x - \sin C_n x), \quad \text{(A13)}$$

where C_n is a solution of $1+\cos C_n \cosh C_n = 0$. The deflection function of the cantilever beam can be expressed as

$$\hat{W}(x|\omega) = \sum_{n=1}^{\infty} \hat{F}_n(\omega)\alpha_n(\omega)\phi_n(x), \quad \text{(A14)}$$

where

$$\alpha_n(\omega) = \frac{2\cos C_n \tan C_n}{C_n(C_n{}^4 - B^4(\omega))(\sin C_n + \sinh C_n)}, \quad \text{(A15)}$$

$$\left|\hat{F}_n(\omega)\right|_s^2 = \frac{3\pi k_B T}{k C_n{}^4 \int_0^{\infty} \left|\alpha_n(\omega')\right|^2 d\omega'}, \quad \text{(A16)}$$

where subscript s refers to the spectral density, $B(\omega)$ is given as

$$B(\omega) = C_1 \sqrt{\frac{\omega}{\omega_{vac,1}}} \left(1 + \frac{\pi \rho b^2}{4\mu}\Gamma(\omega)\right)^{1/4}, \quad \text{(A17)}$$

and spring constant of the beam k is given by

$$k(T) = \frac{3E(T)I}{L^3}. \quad \text{(A18)}$$

For double layered cantilever beam, the fundamental resonance frequency $\omega_{vac,1}$ is given by the Reuss model as [48]

$$\omega_{vac,1}(T) = \omega_{vac}(T)(1+x)^2 \sqrt{\frac{E_a(T)\rho_s}{(E_a(T)+xE_s(T))(\rho_s + x\rho_a)}}, \tag{A19}$$

where $\omega_{vac}(T)$ is the fundamental resonance frequency of the uncoated or single-layered cantilever at T in vacuum, the thickness ratio $x = t_a/t_s$ with t_a being the coating thickness and t_s being the substrate thickness. $E_s(T)$ and $E_a(T)$ represent the Young's modulus of the cantilever substrate and the coated material, respectively. ρ_s and ρ_a are the mass density of the substrate and the coated material, respectively. By integrating both sides of the thermal sensitivity equation for a single layer cantilever [48]

$$\frac{df}{fdT} = \frac{\alpha}{2} + \frac{dE}{2E(T)dT}, \tag{A20}$$

the fundamental resonant frequency in vacuum ω_{vac} is formulated as

$$\omega_{vac}(T) = \omega_{vac}(T_0)\sqrt{\frac{E(T_0) + \frac{dE}{dT}(T-T_0)}{E(T_0)}}\, e^{\frac{\alpha}{2}(T-T_0)}, \tag{A21}$$

where T is the surrounding medium temperature in which the cantilever is submerged and T_0 is the reference temperature. The fundamental resonant frequency at the reference temperature $\omega_{vac}(T_0)$ is provided by the Simple Harmonic Oscillator (SHO) model using the readily measured peak resonance response frequency and the Q-factor in air [41].

Substituting Eq. (A16) into (A14) and noting that all modes are uncorrelated, the

extended Sader's viscous model is obtained as

$$\left|\hat{W}(x|\omega)\right|_s^2 = \frac{3\pi k_B T}{k}\sum_{n=1}^{\infty}\frac{|\alpha_n(\omega)|^2}{C_n^{\,4}\int_0^{\infty}|\alpha_n(\omega')|^2\,d\omega'}\phi_n^2(x), \tag{A22a}$$

$$\left|\frac{\partial\hat{W}(x|\omega)}{\partial x}\right|_s^2 = \frac{3\pi k_B T}{k}\sum_{n=1}^{\infty}\frac{|\alpha_n(\omega)|^2}{C_n^{\,4}\int_0^{\infty}|\alpha_n(\omega')|^2\,d\omega'}\left(\frac{d\phi_n(x)}{dx}\right)^2. \tag{A22b}$$

Equation (A22a) gives the frequency response of the square of the magnitude of the displacement function at all positions along the beam, whereas Eq. (A22b) gives the corresponding result for the slope. It is noted that in AFM applications, the magnitude of the slope is typically measured [i.e., square root of Eq. (A22b)], since deflections of the beam are often obtained using optical detection systems. Equations (A22a) and (A22b) then give the relationship between the frequency spectra of the displacement and slope of the beam.

Recently, the original Sader's viscous model was modified for the theoretical prediction of the frequency response of cantilever beams immersed in viscous fluid near a solid surface by Green and Sader [43]. In addition to the previous assumptions and approximation, a cantilever beam lying parallel to an infinite planar surface is assumed and the spectral density of the thermal driving force which should include the frequency

dependence in the dissipative component of the hydrodynamic force, which was omitted in the previous model, is successfully implemented.

For the important case where the cantilever beam is excited by thermal Brownian motion of the fluid molecules, the frequency response of the magnitude squared of the slope of the displacement function is given by

$$\left|\frac{\partial \hat{W}(x|\omega)}{\partial x}\right|_s^2 = \frac{3\pi k_B T \rho b^2}{k\mu\omega_{vac,1}} \sum_{n=1}^{\infty} \left|\alpha_n(\omega)\right|^2 \omega \Gamma_i(\omega) \left(\frac{d\phi_n(x)}{dx}\right)^2, \tag{A23}$$

where k_B is Boltzmann's constant, T is absolute temperature, ρ is the density of fluid, k is the normal spring constant of the cantilever beam, μ is its mass per unit length, $\omega_{vac,1}$ is the radial resonant frequency of the fundamental mode of flexural vibration of a cantilever beam in vacuum, and the subscripts s and n refer to the spectral density and mode number, respectively. The fundamental resonance frequency $\omega_{vac,1}$ is obtained by substituting Eq. (A21) into (A19). Note that the difference between Eq. (A22b) and Eq. (A23). Frequency response of a cantilever beam lying parallel to a solid surface is directly calculated with one important modification: the hydrodynamic loading due to motion through the fluid must now include the contribution due to the presence of the solid surface.

The hydrodynamic function Γ(ω) for flexural vibrations of a rectangular cantilever beam is of the form

$$\Gamma(\omega) = \Gamma_r(\omega) + i\Gamma_i(\omega), \tag{A24}$$

where

$$\begin{aligned}\log_{10}\Gamma_r(\omega) = {} & a_0 + a_1\tau + a_2\tau^2 + a_3\tau^3 + a_4\tau^4 + a_5\tau^5 + a_6\tau^6 + a_7\tau^7 \\ & + a_8\tau^8 + a_9\tau^9 + a_{10}\tau^{10} + a_{11}\tau^{11} + a_{12}\tau^{12} + a_{13}\tau^{13} + a_{14}\tau^{14} \\ & + a_{15}\tau^{15} + a_{16}\tau^{16} + a_{17}\tau^{17} + a_{18}\tau^{18} + a_{19}\tau^{19} + a_{20}\tau^{20},\end{aligned} \tag{A25a}$$

$$\begin{aligned}\log_{10}\Gamma_i(\omega) = {} & b_0 + b_1\tau + b_2\tau^2 + b_3\tau^3 + b_4\tau^4 + b_5\tau^5 + b_6\tau^6 + b_7\tau^7 \\ & + b_8\tau^8 + b_9\tau^9 + b_{10}\tau^{10} + b_{11}\tau^{11} + b_{12}\tau^{12} + b_{13}\tau^{13} + b_{14}\tau^{14} \\ & + b_{15}\tau^{15} + b_{16}\tau^{16} + b_{17}\tau^{17} + b_{18}\tau^{18} + b_{19}\tau^{19} + b_{20}\tau^{20},\end{aligned} \tag{A25b}$$

and $\tau = \log_{10}(\mathrm{Re})$. The coefficients a_n and b_n for some specified separation distances are provided in reference [43] Tables I and II.

VITA

Seonghwan Kim was born in Seoul, South Korea on November 19, 1974. After graduating from Seoul High School in 1993, he entered Seoul National University in Seoul, South Korea and received a B.S. degree in Aerospace Engineering in 1998 and a M.S. degree in Aerospace Engineering in 2000. After graduation, he joined Korea International Cooperation Agency (KOICA) as a Korea Oversea Volunteer for two years to make a better world. He was dispatched to Indonesia and taught several courses at the Mataram University, one of the state universities in Indonesia. After successfully finishing his work in Indonesia, he came back to South Korea and worked as a research engineer at Digital Bio Technology Co. for one year.

His doctorate study in Mechanical Engineering began at the University of Tennessee, Knoxville in August 2004 and successfully completed all requirements toward his doctoral degree at the Micro/Nano-Scale Fluidics and Energy Transport Laboratory in May 2008. He receives his doctoral degree on August 2008 at the University of Tennessee, Knoxville under the supervision of his primary advisor, Dr. Kenneth D. Kihm, Magnavox Chair Professor, and his co-advisor, Dr. Anthony E. English, Assistant Professor in Mechanical, Aerospace, and Biomedical Engineering Department.